

AD-A063 316

NAVAL RESEARCH LAB WASHINGTON D C

F/G 17/8

SENSITIVITY ANALYSIS OF THE SAGNAC-EFFECT, OPTICAL-FIBER, RING --ETC(U)

NOV 78 S LIN, T G GIALLORENZI

UNCLASSIFIED

NRL-8250

NL

OF
AD
A063316



AD A063316

DDC FILE COPY

12
16.5

NRL Report 8250

Sensitivity Analysis of the Sagnac-Effect, Optical-Fiber, Ring Interferometer

SHIH-CHUN LIN AND THOMAS G. GIALLORENZI
Optical Sciences Division

LEVEL

November 16, 1978

DDC
RECEIVED
JAN 17 1979
A



NAVAL RESEARCH LABORATORY
WASHINGTON, D.C.

Approved for public release; distribution unlimited

9.01 16 103

SECURITY CLASSIFICATION OF THIS PAGE (When Data Entered)

REPORT DOCUMENTATION PAGE		READ INSTRUCTIONS BEFORE COMPLETING FORM
1. REPORT NUMBER NRL Report 8250	2. GOVT ACCESSION NO.	3. RECIPIENT'S CATALOG NUMBER
4. TITLE (and Subtitle) ① SENSITIVITY ANALYSIS OF THE SAGNAC-EFFECT, OPTICAL-FIBER, RING INTERFEROMETER.		5. TYPE OF REPORT & PERIOD COVERED ② Interim report on one phase of a continuing problem.
7. AUTHOR(s) ⑩ Shih-Chun Lin and Thomas G. Giallorenzi		6. PERFORMING ORG. REPORT NUMBER
9. PERFORMING ORGANIZATION NAME AND ADDRESS Naval Research Laboratory Washington, D.C. 20375 62721N		8. CONTRACT OR GRANT NUMBER(s)
11. CONTROLLING OFFICE NAME AND ADDRESS Naval Air Systems Command Washington, D.C. 20361		10. PROGRAM ELEMENT, PROJECT, TASK AREA & WORK UNIT NUMBERS NRL Problem N01-64.301 NAVAIR 62721N, WF21-234-000
14. MONITORING AGENCY NAME & ADDRESS (if different from Controlling Office) ⑭ NRL-8250		12. REPORT DATE November 16, 1978
		13. NUMBER OF PAGES 38
		15. SECURITY CLASS. (of this report) UNCLASSIFIED
		15a. DECLASSIFICATION/DOWNGRADING SCHEDULE
16. DISTRIBUTION STATEMENT (of this Report) Approved for public release; distribution unlimited. ⑪ 16 Nov 78 ⑫ 39 P.		
17. DISTRIBUTION STATEMENT (of the abstract entered in Block 20, if different from Report) ⑬ F21234 ⑭ WF21234000		
18. SUPPLEMENTARY NOTES		
19. KEY WORDS (Continue on reverse side if necessary and identify by block number)		
20. ABSTRACT (Continue on reverse side if necessary and identify by block number) The sensitivity of a recently reported optical-fiber, ring interferometer as a gyro has been analyzed. Photomixing signal-to-noise ratios were derived for the detection schemes using outputs based on both single and complementary fringes. Light-scattering processes, ubiquitous in the optical fiber, such as the Rayleigh, Brillouin, Mie, and core-cladding interface scattering, are assessed quantitatively because they induce, as does the signal, shot noises that set an upper limit to the minimum-detectable rotational rate. Mode stripping is a necessary feature because it can reduce the trapped scattered light level by about a factor of 100. A thorough discussion → next page		

DD FORM 1473
1 JAN 73

EDITION OF 1 NOV 65 IS OBSOLETE
S/N 0102-014-6601

SECURITY CLASSIFICATION OF THIS PAGE (When Data Entered)

254 950

set

20. ABSTRACT (continued):

of the problems and their solutions associated with the dc detector scheme reveals that, in order to achieve the highest photon-noise-limited sensitivity, a nonreciprocal 90° phase bias with phase modulation, or a heterodyne technique, is essential. Optimum gyro sensitivities are discussed via numerical examples in terms of laser input wavelengths and power limits. Results show (a) that a longer wavelength such as 1.1 μm is more desirable than a shorter wavelength such as 0.633 μm because at $\lambda = 1.1 \mu\text{m}$ the fiber's ultimate scattering loss rate is much lower, hence longer fibers can be used to increase sensitivity; and (b) that high-power operation where the only noise is due to stimulated Brillouin scattering gives a better sensitivity than the lower power case. For example, at $\lambda = 0.633 \mu\text{m}$, our calculations give sensitivities of 0.0078 deg/h at 2 mW and 0.0007 deg/h at 14.4 mW. These calculated high-power sensitivities are better than those of current laser ring gyros. Therefore, with adequate research and development, optical-fiber interferometers may be realized as a viable alternative to ring lasers as gyros.

$\lambda = 1.1 \text{ micrometers}$

ABSTRACT for	
RTG	White Section <input checked="" type="checkbox"/>
DDC	Self Section <input type="checkbox"/>
UNCLASSIFIED	<input type="checkbox"/>
JUSTIFICATION	
BY	
DISTRIBUTION/AVAILABILITY CODES	
Dist.	AVAIL. and/or SPECIAL
A	

CONTENTS

INTRODUCTION	1
SIGNAL-TO-NOISE ANALYSIS	2
Operational Description	2
Signal	3
Noise Sources	5
Signal-to-Noise Ratio	6
LIGHT SCATTERING IN OPTICAL FIBERS	10
Distribution Laws	10
Trapping Factors	13
Scattering Coefficients	15
RELATIVE POWER DISTRIBUTIONS AND SIGNAL-TO-NOISE DEGRADATION	19
Relative Power Distributions	19
Signal-to-Noise Degradation	20
PROBLEM AREAS AND THEIR PROMISING SOLUTIONS	21
Need for Stable DC Phase Bias	21
Vulnerability to Low-Frequency Noises	22
Need for High Sensitivity	23
SENSITIVITY LIMITS	26
Optimum Length and Minimum Detectable Rotational Rate at Low Power	26
Effect of Stimulated Brillouin Scattering at High Power	28
CONCLUDING REMARKS	31
ACKNOWLEDGMENTS	33
REFERENCES	33

SENSITIVITY ANALYSIS OF THE SAGNAC-EFFECT OPTICAL-FIBER RING INTERFEROMETER

INTRODUCTION

Recently, R.B. Brown [1], in a study of inertial rate sensing, suggested the use of a Sagnac-effect, fiber, ring interferometer. Through the use of a multiple-turn fiber loop, high sensitivities appeared to be feasible if fiber optic attenuation could be reduced. Since that time (1968), the development of single-mode, extremely low-loss optical fibers [2] has progressed rapidly, making fiber-optic, Sagnac interferometers possible. Vali and Shorthill [3,4] were the first to demonstrate single-fiber interferometer gyro for rotational rate sensing. Fiber interferometers using two fibers represent a second class of devices that appear to be suitable as highly sensitive pressure [5], stress, and temperature sensors. In this report, an analysis describing single fiber interferometer gyros is presented that provides the theoretical sensitivities of these devices in practical situations.

In their first paper, Vali and Shorthill [3] gave a preliminary estimate of fiber interferometer sensitivity; however, their estimate was not intended to completely describe the performance of these devices and consequently did not accurately describe the experimental configurations most commonly encountered. Specifically, they did not take into account the ubiquitous scattered light in the long optical fiber as one of the noise sources. Furthermore, the formula they used to estimate the photon-noise-limited sensitivity of the interferometer was not derived for the experimental optical configurations depicted in their papers; [3,4], but rather, was directly taken from a paper by G.E. Moss, et al. [6]. Moss, et al. considered a heterodyne ac phase-detection technique, whereas the optical detection used by Vali and Shorthill [3,4], was a dc (or homodyne) technique.* The results for an ac detection scheme do not necessarily apply to dc schemes because one has to consider, in each case, different noise sources that affect the outcome of a sensitivity analysis, and hence its conclusions.

This report presents some results of a sensitivity analysis of Sagnac-effect, optical-fiber, ring interferometers with detailed considerations of signals and noises. For simplicity as well as to provide a focus of discussion, the experimental optical fiber configuration proposed by Vali and Shorthill was analyzed and compared. In the following sections, we will first derive pertinent formulas for signal-to-noise ratios, and then discuss noise components due to Rayleigh, Brillouin, Mie, or core-cladding interface light scattering. These will be followed by a discussion of particular problems and promising improvements. Finally, the limiting sensitivities at both low and high input powers are given.

Manuscript submitted June 8, 1978. Resubmitted July 3, 1978.

*The modulation frequency of this interferometer was set as high as 20 kHz so that low-frequency noise effects such as mechanical vibration-induced noise (1/f noise in detection) were eliminated by narrow bandpassing. R.L. Forward has pointed out the inadequacy of using the result of Ref. 6 in a dc detection system (private communication).

The development of a ring interferometer gyroscope that is lightweight, low-cost, and compact offers an alternative to the nearly maturing ring laser gyros and well-matured mechanical gyros, provided that stable, phase biasing techniques can be developed. These biasing techniques described in this report are required so that the gyro can be operated in the region of maximum sensitivity.

SIGNAL-TO-NOISE ANALYSIS

Operational Description

The optical configuration on which the present analysis is based is shown in Fig. 1. The optical source is a single-mode, stabilized, coherent (gas or semiconductor) laser with output power P_0 , and wavelengths in the visible or near-infrared region. The laser output beam is assumed to be well collimated, with uniform phase. As the beam first passes through a lossless beam splitter BS_1 , which has a power reflection coefficient α_1 , its power is attenuated. The transmitted part, $P_0(1-\alpha_1)$, proceeds through a lossless, nondispersive medium and reaches the second beam splitter BS_2 , which is designed to give a 50/50 split of the power at an incident angle of 45° : $(1/2)P_0(1-\alpha_1)$ is the power of the reflected as well as that of the transmitted beam. Each beam is then launched into one end of the single-mode optical-fiber coil of radius R by a focusing lens system, such as a microscope objective, with the optimal f /number to ensure maximum power-coupling efficiency C . In continuous-wave operation, there will be two waves propagating in the whole length L of the fiber simultaneously but in the opposite directions. If the total loss in power through the optical fiber follows the exponential law with an attenuation coefficient α_T (dB/km), and if the loss is reciprocal, i.e., if the loss is the same irrespective of the wave propagation direction, then the power of each emerging beam will be $(1/2)P_0C(1-\alpha_1)e^{-\alpha_T L}$, which we will assume to be 100% intercepted and recollimated by the other focusing lens system. The beam in the clockwise direction (CW) is to undergo one more reflection and the beam in the counterclockwise direction (CCW), one more transmission, before they combine to form a fringe pattern F_1 . The power for each beam is then $(1/4)CP_0(1-\alpha_1)e^{-\alpha_T L}$.

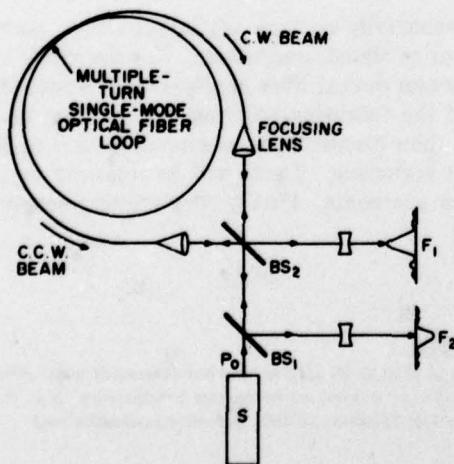


Fig. 1 — Optical setup of the ring interferometer for the analysis

As they continue toward the BS₁, the remaining halves of the beams are reflected from it to form the second fringe pattern F_2 . Their powers will be $(1/4)CP_0\alpha_1(1-\alpha_1)^{-n}r^L$. This fringe pattern, formed by waves that have undergone different numbers and orders of reflections and transmissions from those of F_1 , has a phase, in general, different from that of F_1 . If the difference is 180° , the two fringe patterns are said to be complementary. In what follows, we will assume that this is the case.

A well-adjusted optical system such as this, if in inertial motion, will give rise to two infinite-width fringe patterns that have uniform but different brightnesses. However, as soon as the system is set into rotation, concentric interference rings are formed due to the phase difference between the CW and the CCW waves because of the Sagnac effect [7]. When the rotational axis is parallel to the axis of the optical fiber coil of N turns and of constant loop area A , the phase difference

$$\Delta\phi = \frac{8\pi NA}{\lambda c} \Omega,$$

where λ is the free-space* optical wavelength, c is the free-space speed of light, and Ω is the rate of rotation. For a circular coil, $A = \pi R^2$ and $L = 2\pi RN$; therefore, $\Delta\phi = [4\pi LR/(\lambda c)] \Omega$.† The quantity in the square brackets is the sensitivity of the phase difference to the rotational rate. It is clear in principle that, to increase the sensitivity, we should increase the total length and radius of the coil, and use as short an optical wavelength as possible. However, in practice, packaging criteria limit the size of R ; optical fiber loss sets an upper bound on the length L ; nonlinear damage effects forbid the use of very high power laser sources; and the signal strength, the scattered light, and the quantum efficiency of the detector ultimately limit the system sensitivity. In other words, system tradeoffs must be studied. The sensitivity analysis done below is thus central to the trade-off study.

The Signal

The ring interferometer described above is not sufficient for rotational rate sensing because one has to extract the phase information from the fringe patterns. Although fringe counting techniques [8,9] have been used to extract the phase by spatial sampling of the fringe pattern, they involve either a modification of the interferometer setup or a multisensor fringe locator with rather elaborate electronic logic circuitry. A simpler technique, as shown in Fig. 2, is to use a single photodetector focused on the center of the fringe pattern such that the area in the fringe pattern in the field-of-view of the detector is small compared with the width of a fringe to ensure uniform optical intensity across the detector surface.

The fringe intensity depends on the interference (i.e., coherence) among the optical fields emerging from one end of the fiber and those from the other end. Let E_{tcw} be the sum of all possible optical fields from one end in the CW direction; then, in general, $E_{\text{tcw}} = E_{\text{coh}} + E_{\text{incoh}}$, where E_{coh} represents the sum of coherent optical fields, and E_{incoh} represents that of

*By "free space" here, we mean either a vacuum or a homogeneous nondispersive medium in which the optical system is submerged.

† The fringe shift in a fringe pattern caused by the phase difference $\Delta\phi$ is just $\Delta\phi/2\pi$.

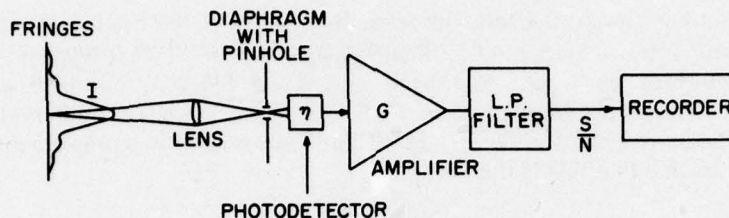


Fig. 2 — Optical mixing technique for the phase difference measurement

the incoherent fields. Similarly, $E_{\text{ccw}} = E'_{\text{coh}} + E'_{\text{incoh}}$, in the CCW direction. Then the instantaneous intensity in the fringe is given by

$$\begin{aligned} I &= E_{\text{cw}} E_{\text{ccw}}^* = (E_{\text{coh}} + E_{\text{incoh}})(E'_{\text{coh}} + E'_{\text{incoh}})^* \\ &= E_{\text{coh}} E_{\text{coh}}^* + E_{\text{incoh}} E_{\text{coh}}^* + E_{\text{coh}} E_{\text{incoh}}^* + E_{\text{incoh}} E_{\text{incoh}}^* \end{aligned} \quad (1)$$

If this instantaneous intensity is allowed to fall onto a detector, it will generate photoelectrons, which in the end produce a current,

$$i = DI, \quad (2)$$

where D is the detector conversion factor. In Eq. (1) or (2), after we take the time average over an interval large compared with the period $T = 2\pi/\omega$, we will get terms of autocorrelations (i.e. intensities) of both coherent and incoherent components, as well as terms involving crosscorrelations between coherent components. The crosscorrelations among the incoherent components, or between coherent and incoherent components, will vanish by definition. Only the crosscorrelations between coherent components carry definite phase information. Therefore, the photocurrent i , after time averaging, will consist of a dc term involving all the intensity terms and an ac term involving sinusoidal functions of phases between interfering coherent beams. (The specialization of this to a detector with finite response time in a ring interferometer will be discussed below.) The photocurrent is then amplified, bandpassed, and integrated. This is the optical mixing technique [10] and is well studied in areas of laser communication systems [11]. We note that this optical configuration does not contain any external modulation. Therefore, the detection is direct current in nature. It differs from the conventional homodyne detection scheme, in that there is no adjustable "reference beam." The beats are formed by signal beams themselves. Because of these special features in the proposed optical configuration, we cannot read out the phase difference directly.

The optical mixing output signal is formed by the two directly transmitted beams. The amplitude of the signal depends strongly on the coherence (spatial and temporal) and polarization states of the two beams. These states, in turn, are influenced by scattered light, optical misalignment due to mechanical vibrations, nonuniform temperature and stress fields in the optical fiber, etc. To simplify the analysis, we assume that the optical components are rigidly

tied down, the temperature and stress fields are homogeneous and stationary, the spatial and temporal coherence of the beams are not degraded when transmitting through the single-mode optical fiber,* and that polarization vectors of the two beams remain aligned.† We may, as alternative, consider that the two beams are unpolarized. We also assume that the scattered-light components are completely uncorrelated with the directly transmitted beams so that the only effect to be considered here is their contribution to the background noise.

Noise Sources

To understand the noise sources that are possibly present, we should consider the following:

1. Scattered light in the optical fiber
2. Shot noise, background noise, thermal noise, generation-recombination noise, flicker or $1/f$ noise, dark current noise, and amplifier noise
3. Fluctuations in the laser light
4. Environmental noise sources such as thermal variations, acoustic agitations, and mechanical vibrations or any other large-scale perturbations such as earth's magnetic field variations, etc.

Sources (1) and (2) are intrinsic because they are not related to any environmental factors. The fluctuations in laser light will cause amplitude modulation in the signal; but, we will see below that using a differential scheme involving the two signals coming from two detectors set in the two fringe patterns can eliminate the common mode of the fluctuations. The scheme is also effective in eliminating all the common-mode environmental noises. This is the salient feature of the optical configuration under consideration. Hence, in what follows, we will concentrate only on the intrinsic noise sources.

The scattered light in the optical fiber consists of various components caused by different scattering mechanisms. Parts of the scattered light are trapped in the core and guided to both ends of the fiber and contribute to the noises; other parts are scattered out of the optical fiber and lost forever. The major linear mechanisms are Rayleigh scattering, Mie scattering, core-cladding interface scattering, and Brillouin scattering.‡ Of all these components, only the Brillouin component has a small frequency shift at the backscattering direction; the rest are oscillating at the same frequency as the input laser beam. Whereas the intensities of the components due to Rayleigh and Brillouin scattering are symmetrically distributed with respect to the forward and backward directions, those due to Mie and core-cladding interface scattering are

*This is certainly not true for a multimode fiber, for it has been observed that speckled patterns are formed at the output of such a fiber.

†For linearly polarized input waves, the output waves from a long, single-mode fiber may acquire some degree of ellipticity in their polarization states due to stress birefringence or deviation of the core cross section from a perfectly circular shape. However, these effects are most likely reciprocal. Therefore, in keeping with the assumption of reciprocity in fiber losses, we feel that it is reasonable at this time to put aside the question on polarization.

‡There is Raman scattering, which has a much larger frequency shift. Because its scattering coefficient is 10 to 20 times smaller than Brillouin scattering, we will not consider it here.

mainly one-sided, i.e., only in the forward direction. Therefore, in the CW direction, we will have, aside from the direct CW beam (its field denoted by E_{CW}), a Rayleigh forward component E_{RF} , a Brillouin forward component E_{B0} , and a strong forward-peaked component (E_{FP}), which are associated with CW beam, and furthermore, a Rayleigh backward component E_{RB} and a Brillouin backward component $E_{B\pi}$, which are induced by the CCW beam traveling in the opposite direction. Thus, we have a total of six fields propagating in the same one direction. Similarly, we have another total of six in the other direction. These are illustrated in Fig. 3.

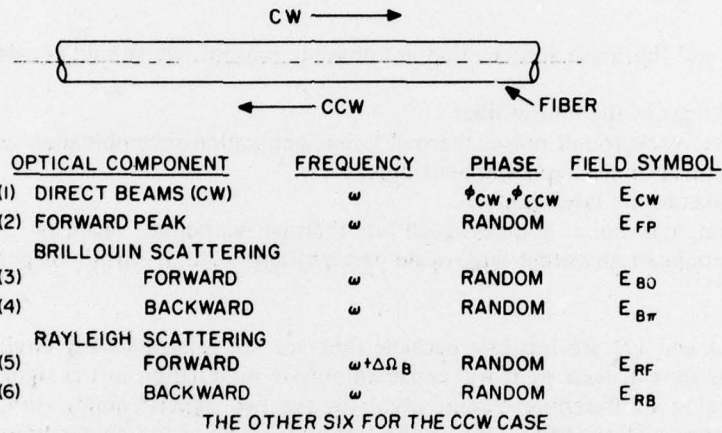


Fig. 3 — Direct optical beams in clockwise (CW) and counterclockwise (CCW) directions in a fiber inducing other scattered components: forward peak, Brillouin, and Rayleigh. Except for the direct beams, the phases of the others are random.

As these scattered-light components are inevitable in the optical wave transmission through any scatter-dominated fibers, and as they are always encountered in complete systems noise analysis, we shall devote, in a separate section, a more detailed discussion to their origin, characteristics, and distribution laws, as well as the magnitudes of their scattering coefficients.

Signal-to-Noise Ratio

The six optical fields in the CW direction will mix with the other six in the CCW direction on the surface of a photodetector placed at the center of the fringe pattern (say, F_1). Since a photodetector is a square-law detector, therefore, there are 36 terms including all the squared and cross-product terms. But, in steady-state, continuous-wave operations, all the scattered component fields will be incoherent (or of random phases) because each is composed of contributions from randomly distributed scattering centers throughout the optical fiber. Since the Brillouin backscattered beams have a frequency shift of the order of 25 GHz, beating between them and the direct beams may occur. But, a beat of 25 GHz is higher than any realistic detector response [12], and it will not be detected. Therefore, the final detector current output, after time-averaging over its time constant τ (where $\tau \gg T = 2\pi/\omega$), as given by

$$\bar{i}_1 = \frac{1}{\tau} \int_0^\tau i_1(t) dt \quad (3)$$

(where the overbar indicates time average and the subscript 1 means photocurrent obtained in fringe pattern F_1), will contain only one cross-term involving the two coherent signal beams. However, the squared terms of all six fields survive the averaging operation and show up in the dc term of the detector current. If the laser fields at the output ends of the fiber are represented by sinusoidal functions $E_{cw} = A_{cw} \cos(\omega t - \phi_{cw})$ and $E_{ccw} = A_{ccw} \cos(\omega t - \phi_{ccw})$, then

$$\begin{aligned} \overline{E_{cw} E_{ccw}} &= \frac{1}{2} \overline{A_{cw} A_{ccw} \cos(\pi + \Delta\phi)} \\ &= -\frac{1}{2} \overline{A_{cw} A_{ccw} \cos(\Delta\phi)}, \end{aligned} \quad (4)$$

where

A_{cw} and A_{ccw} are the amplitudes

ω is the laser circular frequency

t is time

ϕ_{cw} and ϕ_{ccw} are, respectively, the phases associated with the direct CW and CCW traveling waves, and $\Delta\phi = \phi_{cw} - \phi_{ccw}$

π is a phase shift due to reflection from the beam-splitter BS_2 , provided that it has a dielectric surface, and the numerical factor $1/2$ is due to the power reduction upon reflection from or transmission through the BS_2 .

The squared terms of the signal and scattered light are of the same form, i.e.,

$$\overline{E_{cw}^2} = \overline{A_{cw}^2 \cos^2(\theta)} = \frac{1}{2} \overline{A_{cw}^2}. \quad (5)$$

Recalling that the scattering processes are assumed reciprocal so that each scattered component in the CW direction is equal to that in the CCW direction, then, by defining an optical intensity $I \equiv |A|^2$, we get, for the averaged photodetector output current, the expression

$$\bar{i}_1 = D \left[\frac{1}{2} (I_{cw} + I_{FP} + I_{RF} + I_{RB} + I_{B0} + I_{B\pi}) - \frac{1}{2} I_{cw} \cos(\Delta\phi) \right], \quad (6)$$

where

$D \equiv \frac{\eta q}{h\nu}$ is the detector conversion factor with

η = quantum efficiency of the detector

ν = laser frequency

q = electronic charge

h = Planck's constant

and

$$\Delta\phi = \frac{8\pi NA}{c\lambda} \Omega.$$

Clearly, if $\Omega = \text{constant}$, the term that contains $\cos(\Delta\phi)$ is a time-independent signal term. Hence, the detection process is necessarily a dc mode, which can be susceptible to low-frequency noises.

Using a similar argument, if the similar detector system is set at fringe pattern F_2 , we arrive at an expression for the time-averaged photocurrent from detector 2:

$$\bar{i}_2 = D' \alpha_1 \left[\frac{1}{2} (I_{cw} + I_{FP} + I_{RF} + I_{RB} + I_{B0} + I_{B\pi}) + \frac{1}{2} I_{cw} \cos(\Delta\phi) \right], \quad (7)$$

where

α_1 = power reflection coefficient of the BS₁

and

$D' = \frac{\eta' q}{h\nu}$ is the detector conversion factor for detector 2.

Note that the quantum efficiency η' may be different from η of detector 1. The sign change in the last term of Eq. (7) is due to complementarity.

The total photocurrent from each detector is obtained by integrating the intensities of all the light components in the fringe pattern over the small area a that is seen by the detector. Assuming that the optical waves are perfectly aligned and that the quantum efficiency η is uniform across the detector surface, we get total photocurrents for the detectors 1 and 2 as

$$\begin{aligned} i_{T1} &\equiv \int_{a_1} \bar{i}_1 da = Da_1 \left[\frac{1}{2} (I_{cw} + I_{FP} + I_{RF} + I_{RB} + I_{B0} + I_{B\pi}) - \frac{1}{2} I_{cw} \cos(\Delta\phi) \right] \\ &= D \left[\frac{1}{2} (P_{cw} + P_{FP} + P_{RF} + P_{RB} + P_{B0} + P_{B\pi}) - \frac{1}{2} P_{cw} \cos(\Delta\phi) \right] \end{aligned} \quad (8)$$

and

$$\begin{aligned} i_{T2} &\equiv \int_{a_2} \bar{i}_2 da \\ &= D' \alpha_1 \left[\frac{1}{2} (P'_{cw} + P'_{FP} + P'_{RF} + P'_{RB} + P'_{B\pi} + P'_{B0}) + \frac{1}{2} P'_{cw} \cos(\Delta\phi) \right], \end{aligned} \quad (9)$$

where P and P' denote optical powers ($P \equiv Ia$). Here, $P/P' \equiv a_1/a_2$ because $I = I'$. If $a_1 = a_2$, then $P = P'$. In (8) and (9), the first term is the total dc power and the second is the ac signal term. The dc power will produce shot noise. Taking into account the other possible noise sources, the signal-to-noise ratio, based on the *peak* electrical power measured at the load resistor R_L after the total photocurrent being amplified with gain G and filtered at baseband B_o is of the form (according to standard homodyne technique [11]),

$$\left(\frac{S}{N} \right)_{peak} = \frac{D^2 G^2 P_{cw}^2 R_L / 4}{2qG^2 \left[\frac{D}{2} (P_{cw} + P_{FP} + P_{RF} + P_{RB} + P_{B0} + P_{B\pi}) + DP_b + I_D \right] + 4kTB_o} \quad (10)$$

where

P_b = external light induced background noise

I_D = detector dark current or other kinds of current noises depending on the kind of detector used

$4kTB_o$ = the thermal noise term, where with T is the absolute temperature and k is Boltzmann's constant.

If the optical powers are high and the other noises can either be low or eliminated, then we are in a shot-noise- or quantum-noise-limited situation whereby Eq. (10) is simplified to

$$\left(\frac{S}{N}\right)_{\text{peak},1} = \frac{1}{4} \frac{D}{qB_o} \frac{P_{cw}^2}{(P_{cw} + P_{FP} + P_{RF} + P_{RB} + P_{B0} + P_{B\pi})} \quad (11)$$

for detector 1, and similarly,

$$\left(\frac{S}{N}\right)_{\text{peak},2} = \frac{1}{4} \frac{\alpha_1 D'}{qB_o} \frac{P_{cw}^2}{(P_{cw} + P_{FP} + P_{RF} + P_{RB} + P_{B0} + P_{B\pi})} \quad (12)$$

for detector 2. Furthermore, if the components of the scattered light in the optical fiber are all neglected, as was done in Vali and Shorthill [3,4], the peak S/N for a single detector reduces to

$$\left(\frac{S}{N}\right)_{\text{peak}} = \frac{1}{4} \frac{DP_{cw}}{qB_o} = \frac{1}{4} \frac{\eta P_{cw}}{h\nu B_o} \quad (13)$$

which is one-fourth of the S/N for a standard heterodyne technique with a synchronous detector, and one-half of that of the baseband direct-detection technique.*

Next, we discuss a differential scheme for $\Delta\phi$ or, more precisely, $\cos(\Delta\phi)$ measurement. The scheme is illustrated in Fig. 4. As we alluded to earlier, the advantage of this scheme is to eliminate or reject, by subtraction, the common-mode or completely correlated extraneous effects from the two detectors. In doing so, the signal level will double because of the difference in the signs of the two ac terms in Eqs. (8) and (9) above, while the uncorrelated noises will add in the mean-square sense. However, to match or balance the two detectors such that the dc components of the two total photocurrents will completely cancel in subtraction, we must make the coefficients of the two terms in Eqs. (8) and (9) equal. We can accomplish this by selecting η , η' , a_1 , a_2 , and α_1 such that $Da_1 = D'a_2\alpha_1$, yet still keep both a_1 and a_2 small as compared with the central fringe widths. After we do that, the total photocurrent to be amplified is

$$i_s \equiv i_{T2} - i_{T1} = Da_1 I_{cw} \cos(\Delta\phi) = DP_{cw} \cos(\Delta\phi). \quad (14)$$

Let the gain of the differential amplifier be G . The peak signal power is, for a load resistor R_L ,

$$R_L \overline{i_s^2} = D^2 G^2 P_{cw}^2 R_L \quad (15)$$

and the noise power, in the quantum-noise limit, is

$$R_L \overline{i_N^2} = (\overline{i_{N1}^2} + \overline{i_{N2}^2}) R_L G^2 = 2qB_o G^2 R_L D(P_{cw} + P_{FP} + P_{RF} + P_{RB} + P_{B0} + P_{B\pi}), \quad (16)$$

*See Ref. 11, Eqs. (10-45) and (10-13) of Chapter 10.

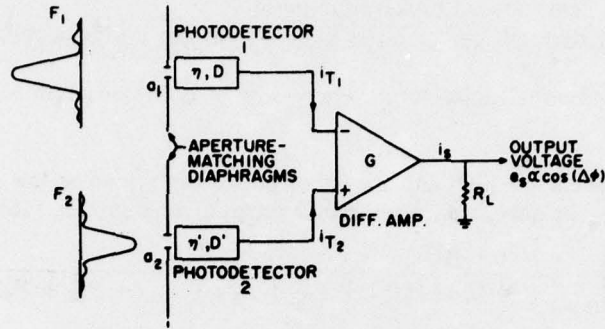


Fig. 4 - Differential detection scheme with balanced inputs to eliminate common-mode noises adaptable to the optical setup of Fig. 1

whence

$$\left(\frac{S}{N}\right)_{\text{peak,diff}} = \frac{\overline{i_s^2}}{\overline{i_n^2}} = \frac{D}{qB_0} \frac{P_{cw}^2}{2(P_{cw} + P_{FP} + P_{RF} + P_{RB} + P_{B0} + P_{B\pi})} \quad (17)$$

Again, if scattering in fiber is neglected, we arrive at

$$\left(\frac{S}{N}\right)_{\text{peak,diff}} = \frac{D}{qB_0} \frac{P_{cw}}{2} = \frac{1}{2} \frac{\eta P_{cw}}{h\nu} \quad (18)$$

Compared with Eq. (13) for a single detector, the differential technique enables us to gain a factor of two in peak electrical power S/N ratio. Equations (11) and (12) give peak S/N for a single detector, and Eq. (17), for the differential scheme, all in the quantum-noise-limited sense. They are correct formulas for the optical configuration shown in Fig. 1 as used by Vali and Shorthill [4], indicating that their formulas would overestimate the sensitivity by a factor of 4.

LIGHT SCATTERING IN OPTICAL FIBERS

As seen from Eqs. (11) or (12), and (17), quantum-noise-limited S/N ratios depend on those scattered-light components that are implicit functions of the fiber length L . In order to see how they depend on L and what their magnitudes are, we need to know, in addition to local scattering coefficients, their distribution laws which would enable us to calculate the cumulative powers at the two ends of an optical fiber of length L . In the following, we shall show how the S/N is degraded by the added scattered light, based on the best available fiber scattering loss data. But, first, let us derive the distribution laws.

Distribution Laws

Direct Beams

By the direct beams we mean those parts of the two optical beams that have not suffered scattering and absorption when propagating through the fiber. Because of the scattering and absorption, which are the main causes for the deletion of optical energy, the direct beam

experiences attenuation. If constancy of the scattering and absorption coefficients and their spatial homogeneity along the fiber are assumed, the law of attenuation of the direct beam will be exponential, i.e.,

$$P(x) = P_i e^{-\alpha_T x}, \quad (19)$$

where P_i is the power of the beam at the input end of the fiber, $P(x)$ is the power in the transmitted beam at a distance x from the input end, and α_T is the total attenuation coefficient which is normally expressed as the sum of the scattering coefficient and the absorption coefficient. Let α_s be the scattering coefficient, and α_{abs} , the absorption coefficient, then we have $\alpha_T = \alpha_s + \alpha_{abs}$.

In applying Eq. (19) to a realistic fiber, we must recognize that (a) the total attenuation coefficient α_T consists of contributions from intrinsic scattering [13–15] and absorption as well as from extrinsic scattering induced by external effects such as bending and vibration of the fiber [16], and that (b) the effect of multiple scattering [17–19] has been neglected.

Scattered Light

Each scattered-light component can be characterized by two parameters; one is the scattering coefficient α_i , where the subscript i indicates the i th kind of scattering process; the other is the factor that quantifies the percentage of trapping of the scattered light in the fiber. We assume that the α_i 's are constant, pursuant to our above discussion, and that the percentage of trapping remains unchanged as the scattered light propagates down the length of the fiber.

The percentage of trapping the forward-scattered power is denoted by F and that of the backward-scattered power, B . We will derive the distribution laws for the forward and the backward components in the single-scattering approximation. This approximation is justifiable, in that the multiple scattering at most will result in only a few percent of the already small scattering losses.

Forward-Scattered Components — The symbols and coordinates of forward scattering are defined in Fig. 5a. The unscattered part of the power reaching a station x from the input end is given by

$$P(x) = P_i e^{-\alpha_T x}.$$

The power scattered from the small element dx is

$$\begin{aligned} dP(x) &= -P(x)\alpha_s dx \\ &= -P_i e^{-\alpha_T x} \alpha_s dx \end{aligned} \quad (20)$$

where α_s = scattering coefficient ($= \alpha_T - \alpha_{abs}$), and the minus sign means a loss. Then the part trapped in the forward direction is

$$dP(x) = -FP_i e^{-\alpha_T x} \alpha_s dx. \quad (21)$$

When this part reaches a downstream station x_1 , its magnitude is reduced by a factor $e^{-\alpha_T(x_1-x)}$. So,

$$\begin{aligned} dP_s(x) &= -FP_i e^{-\alpha_T x} e^{-\alpha_T(x_1-x)} \alpha_s dx \\ &= -FP_i \alpha_s e^{-\alpha_T x_1} dx. \end{aligned}$$

If we integrate dP_s from 0 to x_1 , we obtain all the scattered light produced by the fiber from the input end up to the station x_1 . The integrated result is

$$P_s(x_1) = -FP_s\alpha_s e^{-\alpha_T x_1} x_1. \quad (22)$$

When $x_1 = L$, i.e., the output end of the fiber, we then have the total forward-scattered light

$$P_s(L) = -FP_s\alpha_s e^{-\alpha_T L} L. \quad (23)$$

This is the distribution law for the forward-scattered light.

Backward-Scattered Components — According to Fig. 5b, the scattered power from the small element dx back to a station x_1 with B fraction trapped is

$$\begin{aligned} dP_s(x) &= -BP_s e^{-\alpha_T x} \alpha_s e^{-\alpha_T (x-x_1)} dx \\ &= -BP_s \alpha_s e^{\alpha_T x_1} e^{-2\alpha_T x} dx. \end{aligned} \quad (24)$$

Then the total backscattered light reaching x_1 from the length of fiber $x_1 - L$ is

$$\begin{aligned} P_s(x_1) &= -BP_s \alpha_s e^{\alpha_T x_1} \int_{x_1}^L e^{-2\alpha_T x} dx \\ &= -\frac{BP_s}{2} \frac{\alpha_s}{\alpha_T} [e^{-\alpha_T (2L-x_1)} - e^{-\alpha_T x_1}] \end{aligned} \quad (25)$$

Hence, the total backscattered light arriving at the input end is given by letting $x_1 = L$ in Eq. (25):

$$P_s(0) = -\frac{BP_s}{2} \frac{\alpha_s}{\alpha_T} (e^{-2\alpha_T L} - 1). \quad (26)$$

This is the distribution law for the backscattered light.

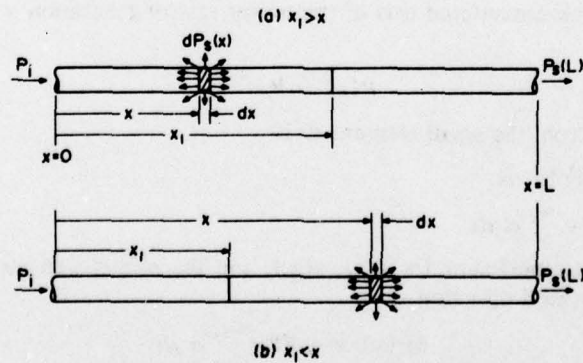


Fig. 5 — Definition of coordinates and scattering fiber elements of the forward scattering (a) and backward scattering (b) processes for the derivation of scattered light distribution laws.

Trapping Factors

For the fundamental mode (HE_{11}) in a single-mode fiber, the power is distributed into the cladding [20,21]. Therefore, when we discuss about the scattered light, in general, we should divide the contribution into two parts: one from the inhomogeneities located randomly inside the core, and the other from those in the cladding. Rays scattered from inside the core that strike the core-cladding interface at an angle larger than the critical angle defined by $\theta_{cr} = \sin^{-1}(n_{clad}/n_{core})$ will be trapped inside the core. Rays striking at an incidence angle $\theta, < \theta_{cr}$ will escape into the cladding and will be either trapped or further escape into the medium surrounding the cladding, depending on whether the index of refraction of the surrounding medium is smaller or larger than that of the cladding, respectively. Some rays initiating from scattering centers in the cladding may be trapped in the cladding if its index of refraction is larger than that of the surrounding, whereas others may refract into the core and be trapped into a helical course. Complications arise if we take into account real effects of the intensity distribution of the HE_{11} mode, mode distortion due to bends in the fiber, and the core-cladding interface irregularities. We will limit our discussion to a simple case where we consider only the more significant scattering components arising from the inhomogeneities distributed in the core and the core-cladding interface. The computation of trapping factors for these components will follow a simple approach by J. Stone [22],* who neglected the scattered light contributed by the cladding. This could be justified by the fact that the intensity of the direct beam in the cladding is much lower than that in the core [20]. To demonstrate the possible influence of all the trapped scattered light in the fiber, we will consider the case where no mode-stripping or index-matching compound is applied on the cladding, together with the more favorable case where mode strippers are used to reduce the cladding trapping.

Since the percentage of the trapped light determines the magnitude of the influence of the scattered light on the ultimate sensitivity of the detection system, we will assess the magnitudes of the trapping factors, F and B . We must note that if there is no trapping, or a very small amount of trapping, then the contribution of scattered light comes only from both ends of the fiber instead of from an integration of all the trapped scattered light along the whole length of the fiber.

Rayleigh and Brillouin Scattering

According to J. Stone [22], the formula for computing the one-way fraction of trapped power, Ω_{trap} , for a bare cladding in air is

$$\begin{aligned} \Omega_{trap} &= \int_0^{2\pi} d\phi \int_0^{\theta_{cr}} (1 + \cos^2 \theta) \sin \theta d\theta \\ &= \frac{4\pi}{2} \left[\frac{4}{3} - \left(\frac{1}{n_{core}} - \frac{1}{3n_{core}^3} \right) \right] \end{aligned} \quad (27a)$$

*A more refined version of the refraction and reflection at the core-cladding interface was given more recently by J.P. Dakin and W.A. Gambling, Opt. Commun. 10, 195-198 (1974). Because we are interested in the first-order effects, we have chosen Stone's formula for symmetric scattering. Dakin and Gambling's formula, which takes into account the effects of depolarization, transverse intensity distribution in the core, and the finite angular width of the propagating interface will, of course, be used when more refined calculations are needed.

where $\theta_0 = \cos^{-1}(1/n_{\text{core}})$ is the limiting scattering angle below which a ray will be trapped in the cladding, n_{core} is the index of refraction of the core material, and the factor $(1 + \cos^2\theta)$ is the angular factor for Rayleigh scattering for unpolarized light. The first term in Eq. (27a) is the fraction of the total Rayleigh scattered power, $\Omega_{\text{total}} = 16\pi/3$.

For a cladding with mode stripper which has an index of refraction higher than that of the cladding, then, light rays with scattering angle close to θ_0 will escape. The amount that will be trapped is determined by the internal refraction at the core-cladding interface, i.e. $\theta_0 = \cos^{-1}(n_{\text{clad}}/n_{\text{core}})$, and Equation (27) becomes

$$\begin{aligned}\Omega_{\text{trap}} &= \int_0^{2\pi} d\phi \int_0^{\theta_0} (1 + \cos^2\theta) \sin\theta d\theta \\ &= \frac{4\pi}{2} \left[\frac{4}{3} - \left(\frac{n_{\text{clad}}}{n_{\text{core}}} - \frac{n_{\text{clad}}^3}{3n_{\text{core}}^3} \right) \right].\end{aligned}\quad (27b)$$

Therefore, the trapping factor F is

$$F \equiv \frac{\Omega_{\text{trap}}}{\Omega_{\text{total}}} = \frac{1}{2} \left[1 - \frac{3}{4} \left(\frac{1}{n_{\text{core}}} + \frac{1}{3n_{\text{core}}^3} \right) \right] \quad (28a)$$

for bare cladding, and

$$F = \frac{1}{2} \left[1 - \frac{3}{4} \left(\frac{n_{\text{clad}}}{n_{\text{core}}} + \frac{n_{\text{clad}}^3}{3n_{\text{core}}^3} \right) \right] \quad (28b)$$

for a mode-stripped or index-matched cladding. Because of symmetry of the Rayleigh scattering, the backward trapping factor B is equal to F . According to J. Schroeder, et. al. [23], Brillouin scattering has the same spatial angular distribution as the Rayleigh scattering. The trapping factors for Brillouin scattering are, therefore, identical to the Rayleigh. For given materials of core and cladding, the trapping factors can be evaluated. For example, let us consider an optical fiber with fused silica core ($n_{\text{core}} = 1.4585$) and a borosilicate glass cladding ($6\text{SiO}_2:1\text{B}_2\text{O}_3$) with an index of refraction about 0.3% less than that of pure fused silica (at $\lambda = 1.06 \mu\text{m}$, $n_{\text{clad}} = 1.4541$). The limiting scattering angle $\theta_0 = 46.7^\circ$ and 4.44° for the bare cladding and index matched cladding, respectively. Based on Eq. (28a), $F = B = 0.2$ and 2.3×10^{-3} , corresponding to the respective θ_0 . We can immediately draw the conclusion that the fiber to be used in a ring interferometer should be equipped with mode strippers, or index-matching components, to reduce the trapping factors by about 100 times for the Rayleigh as well as the Brillouin-scattered components.

Mie and Forward Peak Scattering

In the study of light scattering in the optical fibers, a strong forward scattering component has been observed both for a single mode fiber [24] and a multimode fiber [25]. These peaks were observed just outside the cladding when the fibers were immersed in index-matching fluid. This peak cannot be explained by Rayleigh scattering theory and is generally thought to be caused by two factors: namely, the Mie scattering and the scattering due to core-cladding interface corrugation. Mie scattering was first studied by Rawson [26] for a bulk glass with imbedded spherical particles. These micron-size particles are the homogeneities frozen in during solidification [27]. However, inasmuch as these spherical particles are liable to be drawn

into filaments aligned with the fiber during the fiber-drawing process, Rawson devised a theory for light scattering due to randomly distributed, but aligned, filaments in a fiber [28]. On the other hand, the interface scattering process was first studied theoretically by Marcuse [29]. Since then, there have been more studies [30–33], but none is experimental, presumably because of the difficulties involved in measurements. Experimentally, it is very difficult to separate these two contributions [24,25]. Nevertheless, experimental results do establish the ratios of the total forward-scattering component to the Rayleigh component after other leaky modes are stripped. We will use these ratios to calculate the forward-peak scattering component from the knowledge of the Rayleigh scattering.

It is also conceivable that these losses are dependent on the fiber drawing processes, hence are variable from case to case. But, in order to render some degree of generality for analysis sake, we will assume that the ratios mentioned above will stay constant from fiber to fiber, provided that the fibers are drawn by a similar process from similar preforms.

Our current knowledge of a fiber's ability to trap the forward-peak scattering is too limited to enable us to quantitatively assess the trapping factor for a general case. For example, the question of how much of the forward peak will be guided by the fiber when heavily mode stripped does not have an answer; so it is with the question about the effects of fiber bending on the propagation of the peak, for all the measurements so far have been for a short, straight section. However, because a strong forward peak is observed *outside* of the fiber when immersed in an index-matching fluid, we see clearly that proper mode stripping would eliminate at least a large portion of the forward-peak scattering component. To demonstrate how high the forward peak would be if fully trapped, we will discuss this case in detail. This will be followed with a discussion of a case wherein all the forward peak is assumed to have been removed from the fiber.

The trapping factors for the former case are $F = 1$ and $B = 0$, whereas the trapping factors for the latter case are $F = 0$ and $B = 0$. Of course, in the latter case, we no longer speak of a distribution law. Instead, we should consider the part that is scattered from the exit face of the fiber, which depends on the end-surface conditions.

Scattering Coefficients

As a basis for our discussion, we choose a fiber that has a total loss rate of 4 dB/km at $\lambda = 0.633 \mu\text{m}$. We further assume that the total loss rate is due purely to scattering, in that the absorbing centers in the glass fiber [34] can be completely removed with advanced techniques. In other words, we are considering here a fiber that has a loss mechanism in the frequency range of interest due to scattering alone. We will use a weakly guiding fiber as defined by Gloge [21] that has a fused silica core for quantitative assessment of scattering coefficients.

Brillouin Scattering Coefficient

Rayleigh and Brillouin scattering in glass have been studied extensively in the past [23,35–38]. But, it seems that no detailed study of Brillouin scattering from an optical fiber has been reported in the literature, except the work by Rich and Pinnow [39], which reported the measurements of Brillouin scattering from both the core and the cladding of multimode borosilicate-pure fused silica waveguide, and that of E.M. Dianov, et al. [40]. Brillouin scattering from a single-mode fiber is still lacking. In view of this, we will use formulas for bulk material to calculate Brillouin scattering for the single-mode fiber.

According to Rich and Pinnow, the Brillouin scattering coefficient is given by the formula,

$$\alpha_{SB} = \left(\frac{8}{3} \right) \left(\frac{\pi^3}{\lambda^4} \right) kT \left(\frac{n^8 p_{12}^2}{\rho V^2} \right), \quad (29)$$

where λ is the optical wavelength in free space, k is Boltzmann's constant, T is the absolute temperature, n is the index of refraction of the glass, p_{12} is the applicable photoelastic tensor component, ρ is the density, and V is the longitudinal mode acoustic velocity. For fused silica, they give 0.40 dB/km* for α_{SB} at room temperature and $\lambda = 0.5145 \mu\text{m}$. According to J. Schroeder, et al. [23], the Brillouin scattering coefficient can be obtained through the Rayleigh ratio evaluated at 90° , i.e., $\alpha_{SB} = (8\pi/3) R_{90^\circ}$ for linearly polarized light, where the Rayleigh ratio R_{90° is

$$R_{90^\circ} = \frac{\pi^2}{\lambda^4} (n^8 p_{12}^2) kT (\rho V^2)^{-1}. \quad (30)$$

Equation (30) gives an α_{SB} identical to Eq. (29). If we use the thermophysical and optical data of SiO_2 provided by J. Schroeder, et al. [23] in Tables 1-3 namely, $V = 5.92 \times 10^5 \text{ cm/s}$, $\rho = 2.211 \text{ g/cm}^3$, $p_{12} = 0.286$, $T = 293\text{K}$, $n = 1.458$, and $\lambda = 0.633 \mu\text{m}$, we get $R_{90^\circ} = 0.538 \times 10^{-7} \text{ cm}^{-1}$; hence $\alpha_{SB} = 0.195 \text{ dB/km}^*$ for the $V-V$ polarization component. For the unpolarized light under consideration, α_{SB} is twice as large: $\alpha_{SB} = 0.39 \text{ dB/km}$, which compares well with the value 0.4 dB/km given by Rich and Pinnow for $\lambda = 0.5145 \mu\text{m}$. In what follows, we will use the value 0.40 dB/km as the intrinsic Brillouin scattering loss for the fiber at $\lambda = 0.633 \mu\text{m}$.

Effective Forward-Peak Scattering Coefficient

From experimental results, Rawson [24] established that, for the particular single-mode fiber, out of the total scattering loss rate of about 10 dB/km at $\lambda = 0.633 \mu\text{m}$, the forward peak took a share of 2.5 dB/km, while the Rayleigh scattering, the balance, about 7.5 dB/km. The ratio of the forward peak over the Rayleigh scattered light is about 1:3. In the same paper, Rawson also established that the spectral dependence of the Rayleigh component follows the $1/\lambda^4$ law within 7%. The results measured at $\lambda = 1.06 \mu\text{m}$ show a total loss of about 1.05 dB/km, with forward peak about 0.17 dB/km and Rayleigh component about 0.88 dB/km. The ratio is about 1:5, instead of 1:3. It is interesting to note that the forward peak may not obey the $1/\lambda^4$ law, indicating that the forward peak could be caused by effects other than the Rayleigh scattering.

The same kind of measurement was again carefully done by Reeve, et al. [25] with a multimode fiber. They reported a residual forward peak constituting about one-fifth of the Rayleigh scattered power at $0.633 \mu\text{m}$, and attributed the cause to large-scale (w.r.t. the wavelength) imperfections. They also found the $1/\lambda^4$ characteristics associated with the scattered loss after the forward peak had been subtracted out. Therefore, in our calculations, we will adopt a value of 1:5 for the ratio of the forward peak power over that of the total Rayleigh

*Rich and Pinnow did not give the polarization state of the light when giving the value 0.4 dB/km. Our calculations based on their formula (Eq. 1) and Schroeder's result in values only one-half of it if linear polarization is assumed. We conclude that 0.4 dB/km would be correct for unpolarized light, which is what we presume now.

†1 $\text{cm}^{-1} = 4.33 \times 10^5 \text{ dB/km}$ is the conversion factor.

component. Using this ratio, we are able to ascribe an effective scattering coefficient for the forward peak from the Rayleigh scattering coefficient.

Partition of Scattering Losses

Since Brillouin scattering is intrinsic, we will let it be constant. The total loss is assumed to be 4 dB/km; the Rayleigh scattering and the forward peak scattering are, then, partitioned according to the formulas

$$\alpha_{FP} = (1/5) \alpha_{SR}$$

and

$$\alpha_{SR} = \alpha_T - \alpha_{SB} - \alpha_{FP} \quad (31)$$

where α_{FP} is the equivalent scattering coefficient for the forward peak, which is one-fifth of the total Rayleigh scattering components as we established above. Since $\alpha_T = 4 \text{ dB/km} = 9.24 \times 10^{-7} \text{ cm}^{-1}$ and $\alpha_{SB} = 0.4 \text{ dB/km} = 92.4 \times 10^{-7} \text{ cm}^{-1}$ for $\lambda = 0.633 \text{ } \mu\text{m}$, therefore, by Eq. (31), we get, $\alpha_{FP} = 13.86 \times 10^{-7} \text{ cm}^{-1}$ and $\alpha_{SR} = 69.3 \times 10^{-7} \text{ cm}^{-1}$. Also, $\alpha_{SR}/\alpha_T = 0.1$ and $\alpha_{FP}/\alpha_T = 0.15$.

For comparison, we also calculate these scattering coefficients for $\lambda = 1.1 \text{ } \mu\text{m}$. The reasons for choosing this wavelength will become clear later on. We use the fact that the Rayleigh scattering coefficient scales as $1/\lambda^4$, and the fact that the forward peak scales as $1/\lambda^3$, as established by Rawson [24,28]. Also, according to Rawson's measurements [24] for $\lambda = 1.06 \text{ } \mu\text{m}$, the forward peak is about 0.17 dB/km, whereas the Rayleigh is 0.88 dB/km. The ratio of Rayleigh scattering over the forward peak is 5.18. So, for $\lambda = 1.1 \text{ } \mu\text{m}$, this ratio is about 5.0. Therefore, the forward peak is still one-fifth of Rayleigh component. The Brillouin scattering coefficient also scales as $1/\lambda^4$, as can be seen from Eq. (29). Its value for $\lambda = 1.1 \text{ } \mu\text{m}$ is now 0.043 dB/km. To calculate all the other scattering components, we assume that the ratio between the Brillouin and the Rayleigh components remains unchanged when the wavelength is changed from 0.633 μm to 1.1 μm ; i.e., $\alpha_{SB}/\alpha_{SR} = 1/7.5$. Hence, in conjunction with the condition $\alpha_{FP} = (1/5)\alpha_{SR}$, we get $\alpha_T \approx 0.431 \text{ dB/km}$ and $\alpha_{FP} = 0.065 \text{ dB/km}$ for $\alpha_{SR} = 7.5 \times \alpha_{SB} = 0.323 \text{ dB/km}$. The percent ratios are: $\alpha_{SB}/\alpha_T = 0.1$, $\alpha_{SR}/\alpha_T \approx 0.751$, and $\alpha_{FP}/\alpha_T \approx 0.149$. The value of α_T represents a realistic assessment of the intrinsic scattering loss. It is approached by the current, rapidly advancing fiber manufacturing technology.² We also note that the total loss rate does not scale as λ^{-4} if the cladding mode is not stripped² and if the forward peak contributes significantly.

Because the index of refraction of the fused silica changes very little in the wavelength range 0.5 – 1.3 μm [41,42], the fiber trapping factors, as a weak function of the index of refraction of the core, n_{core} , do not change appreciably. Therefore, we will use the same trapping factors for both wavelengths.

For readers' convenience, we conclude this chapter by summarizing the useful information in Table 1.

Table 1 — Summary of Light Scattering Information in a Typical Fused Silica Fiber

Component	Direction (cw)	Trapping Factors		Attenuation Cross Sections		Distribution Laws (L = fiber length)
		Bare Cladding	Mode Stripping	$\lambda = 0.633 \mu\text{m}$	$\lambda = 1.1 \mu\text{m}$	
Direct beam	Forward only	100% of what is coupled in	100%	—	—	$P_{cw} = P_i e^{-\alpha T L}$
Rayleigh	Forward	$F \cong 0.2$	2.3×10^{-3}	$\alpha_{SR} =$		$P_{RF} = F P_i \alpha_{SR} L e^{-\alpha T L}$
	Backward	$B \cong 0.2$	2.3×10^{-3}	$6.93 \times 10^{-6} \text{ cm}^{-1}$	$7.46 \times 10^{-7} \text{ cm}^{-1}$	$P_{KB} = B P_i \frac{\alpha_{SR}}{2 \alpha_T} [1 - e^{-2 \alpha T L}]$
Brillouin	Forward	$F \cong 0.2$	2.3×10^{-3}	$\alpha_{SB} =$		$P_{BO} = F P_i \alpha_{SB} L e^{-\alpha T L}$
	Backward	$B \cong 0.2$	2.3×10^{-3}	$9.24 \times 10^{-7} \text{ cm}^{-1}$	$0.993 \times 10^{-7} \text{ cm}^{-1}$	$P_{B\pi} = B P_i \frac{\alpha_{SB}}{2 \alpha_T} [1 - e^{-2 \alpha T L}]$
Forward peak	Forward only	$F = 1$	< 1	$\frac{1}{5} \alpha_{SR}$	$\frac{1}{5} \alpha_{SR}$	$P_{FP} = 1 \cdot P_i \frac{\alpha_{SR}}{5} L e^{-\alpha T L}$
				Total = $\Sigma \alpha_T = 9.24 \times 10^{-6} \text{ cm}^{-1}$ = 4 dB/km	$9.95 \times 10^{-7} \text{ cm}^{-1}$ = 0.431 dB/km	

RELATIVE POWER DISTRIBUTION AND SIGNAL-TO-NOISE DEGRADATION

With the scattering losses and trapping factors determined above, we can now evaluate numerically the relative power distribution laws of all the light components in a fused silica fiber of length L . Also evaluated will be the degradation factor of the S/N ratio associated with fiber scattering losses.

Relative Power Distributions

The relative power distribution laws, for fiber with bare cladding, take the following forms (one way only):

$$P_{cw}/\Pi = P_{ccw}/\Pi = e^{-\alpha_r L}$$

$$P_{FP}/\Pi = \left(\frac{1}{5} \alpha_{SR} \right) L e^{-\alpha_r L}$$

$$P_{RF}/\Pi = (0.2 \alpha_{SP}) L e^{-\alpha_r L}$$

$$P_{RB}/\Pi = (0.1 \alpha_{SR} / \alpha_r) [1 - e^{-2\alpha_r L}]$$

$$P_{BO}/\Pi = (0.2 \alpha_{SB}) L e^{-\alpha_r L}$$

$$P_{B\pi}/\Pi = (0.1 \alpha_{SB} / \alpha_r) [1 - e^{-2\alpha_r L}], \quad (32)$$

where L is the total length of the fiber coil, Π is a normalization factor, $\Pi = (1/4)(1 - \alpha_1) P_0 C$. As described in Chapter 1, the decimal numerical coefficients are trapping factors. The reader is reminded of the fact that, in Eq. (32), the backscattered components P_{RB} and $P_{B\pi}$ are due to the wave traveling in the opposite direction to that of the other components. The values of these scattering coefficients are given in column 4, Table 1, for both $\lambda = 0.633 \mu\text{m}$ and $\lambda = 1.1 \mu\text{m}$. We have evaluated Eq. (32) as a function of L . The results are plotted in Fig. 6. We see that the forward-scattering components first increase with L and then reach maxima at $L = L_{\text{max}}$. After that they decay continuously, whereas the backscattered components increase continuously with L and tend to saturate for large L . The direct signal beams are, of course, straight lines in the semilog plot. At $L \gg L_{\text{max}}$, the background noise will be contributed mainly by backscattered light. The Brillouin components are a factor of 7.5 below the Rayleigh and forward peak components (the forward peaks coincide incidentally with the Rayleigh forward components). Since the total scattering loss rate for $\lambda = 1.1 \mu\text{m}$ is about 10 times less than that for $\lambda = 0.633 \mu\text{m}$, the direct beam is obviously decaying much more slowly. The scattered components, in this case, change with L at a much slower rate, although interestingly, they saturate to the same levels at large L as they would for $\lambda = 0.633 \mu\text{m}$. We see also that by going to a longer wavelength, we gain a wider range of fiber length within which we can achieve certain specific sensitivity requirements by using 10- or 20-km lengths of fiber without large degradation in S/N ratios. We conclude that, from the standpoint of scattering losses, we

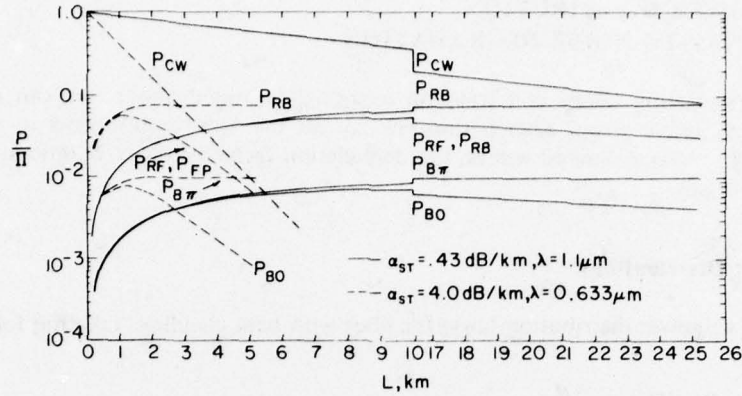


Fig. 6 — Distribution laws for all the scattering components considered for a fiber with attenuation coefficients $\alpha_T = 0.43$ dB/km at $\lambda = 1.1 \mu\text{m}$ (solid lines) and $\alpha_T = 4$ dB/km at $\lambda = 0.633 \mu\text{m}$ (broken lines). Due to attenuation, the forward scattered light components rise first as fiber length is increased, reach maxima, and then decay, whereas the backscattered components rise continuously to saturation. The direct beam attenuates much more slowly in the case $\lambda = 1.1 \mu\text{m}$ than that for $\lambda = 0.633 \mu\text{m}$, while backscattered noises saturate to about the same level.

should prefer $1.1 \mu\text{m}$ to $0.633 \mu\text{m}$ as the light source wavelength. With mode stripping, all the scattered-light components will have magnitudes lower by about a hundredfold except the forward peak, whose reduction due to mode stripping is not absolutely known.

Signal-to-Noise Degradation

To evaluate the degradation of S/N , we take, as an example, the single-detector case. The expression for S/N (from Eq. (11)) is

$$\left(\frac{S}{N} \right)_{\text{peak}} = \frac{1}{4} \frac{\eta}{h\nu B_0} \frac{P_{cw}^2}{P_{cw} + P_{FP} + P_{RF} + P_{RB} + P_{B0} + P_{B\pi}} = Kf(L) \quad (33)$$

where $K \equiv (1/4)\eta/h\nu B_0$ is a constant independent of the fiber length, L , and $f(L) = P_{cw}/(1 + P_N/P_{cw})$ is a complicated function of L , with P_N the sum of the five scattered components.

Physically, $f(L)$ represents the S/N ratio degradation factor due to light scattering in the optical fiber with length L , and KP_{cw} is the S/N ratio if scattered light components are neglected as did in Vali and Shorthill [3]. With the distribution laws as given by Eq. (32) above, we have evaluated $f(L) = (S/N)_{\text{peak}}/K$. The results are plotted in Fig. 7. Curve 1 is for $\lambda = 1.1 \mu\text{m}$ and Curve 2 is for $\lambda = 0.633 \mu\text{m}$. The degradation of S/N in the case $\lambda = 0.633 \mu\text{m}$ can by no means be neglected. The degradation in the case $\lambda = 1.1 \mu\text{m}$ is, by contrast, very mild. This is another reason for adopting a longer wavelength. With mode stripping, of course, the degradation is much less serious.

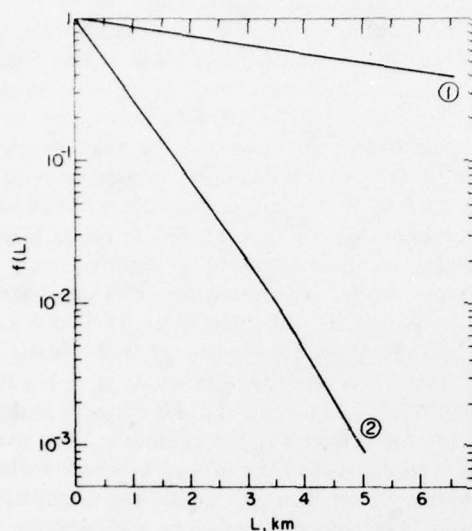


Fig. 7 — Signal-to-noise degradation due to scattered light components in a fiber as a function of optical fiber length L . For a perfect fiber with zero loss, the S/N is purely signal quantum-noise limited and is equal to 1 here. Curve (1) is for $\lambda = 1.1 \mu\text{m}$ (0.43 dB/km); Curve (2), for $\lambda = 0.633 \mu\text{m}$ (4 dB/km). So, at longer wavelength, the degradation is much less significant.

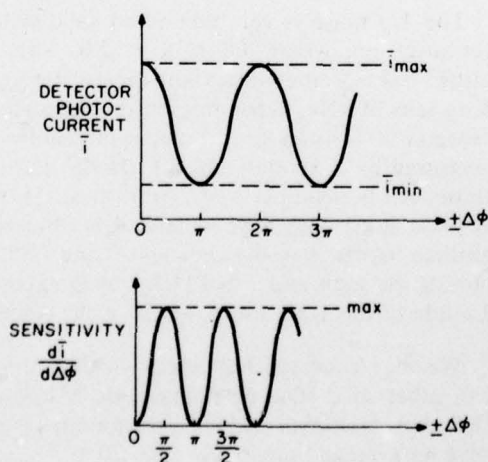
PROBLEM AREAS AND THEIR PROMISING SOLUTIONS

From the preceding analyses and discussions, three problem areas have emerged, mainly due to the stationary nature of the proposed optical arrangement and the homodyne detection schemes.

Need for Stable DC Phase Bias

The first problem area is associated with the fact that the ac term of the photodetector current (i.e. the signal) is proportional to $\cos(\Delta\phi)$; e.g., see Eq. (8). This function has least sensitivity at small values of $\Delta\phi$, since the sensitivity is proportional to $dI_{ac}/d(\Delta\phi)$. As seen in Fig. 8, the central fringe intensity has a maximum sensitivity in phase shift at $\Delta\phi = \pi/2$ or

Fig. 8 — The variation of the photodetector current as a function of the phase difference between the two signal beams. Maximum sensitivity points correspond to the points on the photodetector current curve where its slope has maximum values. Therefore, for small $\pm \Delta\phi$, we need a dc phase bias of $\pi/2$, in order to ensure maximum sensitivity.



$3\pi/2$. In order to ensure the location of $\Delta\phi$ at these points, we must, therefore, provide a constant dc phase bias. Since there are two oppositely travelling waves, we must use nonreciprocal elements based on the well-known Faraday effect [43] to introduce phase biases. The Faraday effect has been well demonstrated in magneto-optical components such as optical isolators. Very compact ones have been reported either for the visible [44] or infrared [45] region of the optical spectrum. While many magneto-optical materials [46] are available, the most promising one is represented by yttrium iron garnet ($\text{YIG}, \text{Y}_3\text{Fe}_5\text{O}_{12}$) which has good transparency in the 1-4- μm region and high Faraday rotation (≈ 250 deg/cm @ 1.1 μm). Isolators without polarizers (45° Faraday rotator) constitute the basic elements that provide the 90° dc phase bias for the ring interferometers. We can obtain a 45° Faraday rotation by using an approximately 2.3-mm-long YIG crystal at 1.25 μm wavelength. Even smaller absorption loss and anomalously larger Faraday rotation than the YIG have been measured by Takeuchi et al. [47] in a single crystal of bismuth-substituted gadolinium iron garnet ($\text{Gd}_{2-x}\text{Bi}_x\text{Fe}_5\text{O}_{12}$ ($x = 0-1.4$)). For example, they report Faraday rotation of more than 3×10^3 deg/cm at $\lambda = 1.1$ μm in $\text{Gd}_2\text{BiFe}_5\text{O}_{12}$ with even less absorption loss than YIG. Such large specific rotation makes it very promising to develop miniaturized components for compact interferometers. The availability of such good characteristics in these garnets, coupled with fiber loss as low as 0.5 dB/km at 1.1 μm , the newly developed GaInAsP/InP double heterostructure diode lasers emitting at 1.1 μm at room temperature, reliable cw operation [48], and Ge avalanche photodiodes with 50% quantum efficiency for $\lambda = 0.6-1.65$ μm [12], indicate clearly the desirability of using long wavelengths in ring interferometric gyros. Similar considerations have prompted Kimura and Daikoku [49] to propose a low-loss 1.0- to 1.4- μm region for future optical fiber communications systems.

Vulnerability to Low-Frequency Noises

The second problem is due to the dc nature of typical optical detection scheme discussed above. As such, it is vulnerable to those very low-frequency noises associated with the detectors and electronics, because we cannot subtract them out through the differential schemes due to their lack of correlations. These low-frequency noises include $1/f$ -type noise, generation and recombination noise, partition noise, etc., with $1/f$ -type noise the most detrimental [50,51]. Therefore, we will only discuss the $1/f$ noise effect.

The $1/f$ noise is common to all solid-state devices. It is a type of noise that has a $1/f^\alpha$ power spectrum, where $0.8 < \alpha < 2.0$, with $\alpha \approx 1$ the most probable value. The $1/f$ noise spectrum has extremely low frequencies; the high-end cutoff, however, can vary from less than 1 Hz to tens of kHz, depending on the detectors. To illustrate this, we show in Fig. 9, two typical spectra of $1/f$ noises: the upper one shows $1/f$ noise associated with the InAs photodiode, as measured by J. Hanlon and S.F. Jacobs [52], and the lower one that of the RCA 1P28 photomultiplier, as obtained by C. Smit et al. [53]. We see that (a) the photomultiplier and the InAs photodiode both have wideband $1/f$ noises, (b) at low-frequency ends, they are orders of magnitude higher than the shot noise, and (c) the photomultiplier shows a very low cut-off frequency at the high end (< 0.1 Hz) of the spectrum. It may be noted that at $f \approx 0.3$ Hz, the magnitude of the $1/f$ noise power is of the same order as that of the shot noise.

We may conclude that the $1/f$ noise is not too serious if the photomultiplier is used in lieu of other solid state detectors in dc or homodyne detection schemes, provided that the size of the photomultiplier can be accommodated in a system and that the measurements do not involve an average time longer than 20 s.

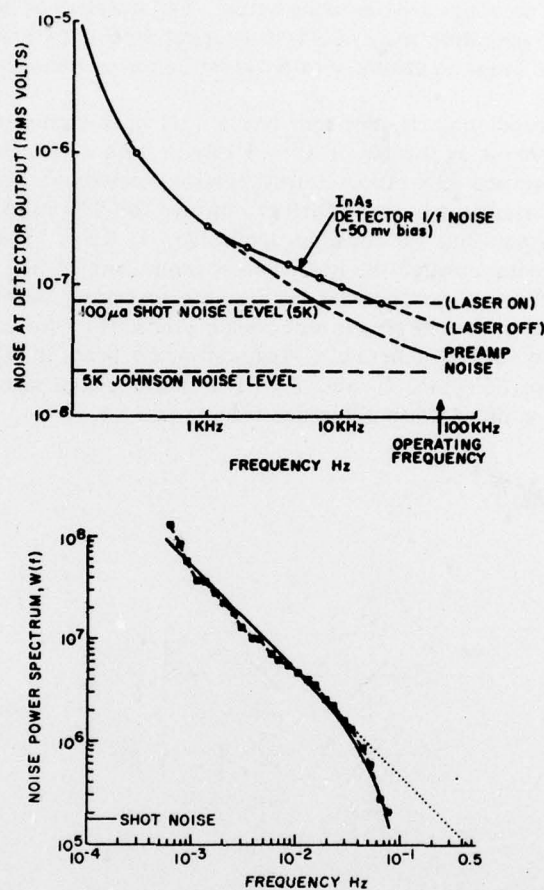


Fig. 9 — Typical solid-state detector noise spectrum (upper figure, InAs, Ref. 52), and photomultiplier noise spectrum (lower figure, Ref. 53) showing the effect of $1/f$ noise at low frequency ends.

However, if we demand that the size of a ring interferometer rate gyro be as compact as a practical ring-laser gyro, then we must select an avalanche photodiode to replace a photomultiplier because an avalanche photodiode can be much smaller in physical size and has the same internal high gain as the photomultiplier. In general, the nonstationarity of the statistics of the $1/f$ noise [54] does not permit the long averaging time often required in slowly varying phenomena. Under these circumstances, the discussed optical scheme will fail to give a high degree of sensitivity. This leads to the third problem.

Need for High Sensitivity

The third problem is the need to achieve a high degree of sensitivity. To this end, we must modify the optical scheme either to incorporate some kind of modulation technique into

the homodyne setup or to adopt a heterodyne setup. The purpose of both modifications is to defeat the $1/f$ noise by operating the system at a higher frequency (carrier frequency is now shifted away from the dc limit) to ensure shot-noise-limited performance.

In the case of heterodyning, Hanlon and Jacobs [52] have demonstrated the feasibility of using a bandwidth as narrow as 0.5 Hz at $\lambda = 1.15 \mu\text{m}$ with a 50-kHz phase modulation to achieve the shot-noise-limited S/N ratio. A true heterodyne scheme also has the capability of providing a strong local oscillator beam to further improve the S/N ratio. Figure 10 shows one of the heterodyne schemes that we consider applicable. It has a local oscillator beam (frequency) which, after passing through the first acoustic modulator (A.M.), where it is modulated at frequency ω_2 , is split into a zeroth order beam and a first-order beam at $\omega_L - \omega_2$, ω_L being the laser frequency. The unshifted zeroth order beam proceeds to the second acoustic modulator, modulated at ω_1 , to further generate a Bragg-diffracted beam at $\omega_L - \omega_1$. Optical mixing occurs at the surfaces of detectors D_1 and D_2 . The demodulated signals are then sent to a phase meter to produce a direct phase difference reading of $2\Delta\phi$.

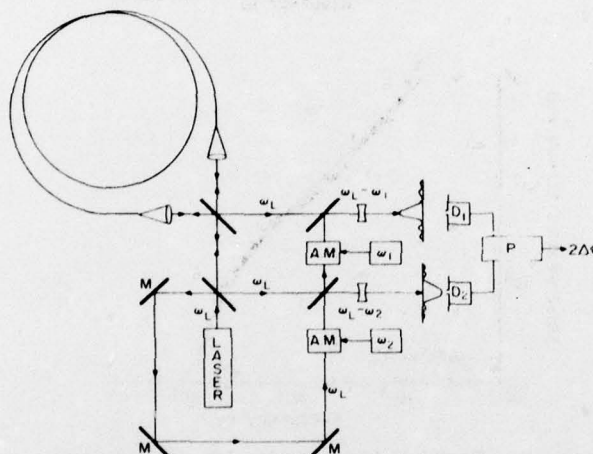


Fig. 10 — An example of ac detection scheme for improvement of the ring interferometer sensitivity: A heterodyne technique evolving from the basic dc configuration shown in Fig. 1.

To illustrate the modulation with homodyne scheme as shown in Fig. 11, we propose to use magneto-optical modulators to provide (a) the dc 90° bias as discussed earlier, and (b) an additional modulation around $\Delta\phi = \pi/2$ by imposing a sinusoidal signal ΔB with a proper amplitude such that the modulation is linear in ϕ . An alternative to (a) and (b) is to use a single large ac modulation, producing a phase shift up to π , and then to count and record the maxima in the output signal. Each maximum corresponds to the phase shift being scanned across $\pi/2$, the maximum sensitivity point. Pursuant to the desirable use of near-infrared wavelengths, we point out that many promising magneto-optical modulators based on Faraday effect have been devised and are ready for adoption here [55]. We emphasize that only through modulation, i.e., ac operation, can the formula given by Moss, et al. [6] relating the sensitivity to the photon noise be used. In the dc bias case, the challenge is to maintain the dc bias to the highest possible stability.

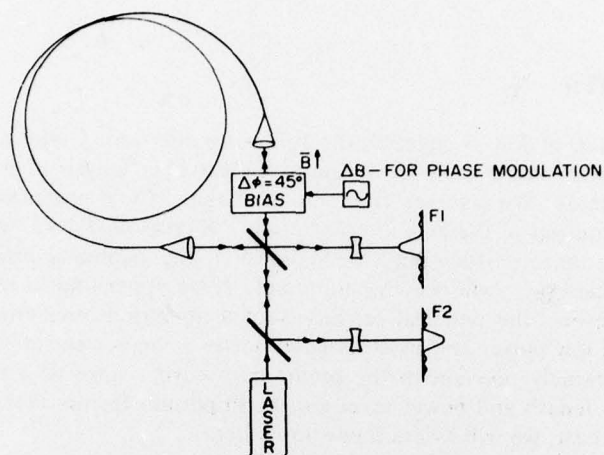


Fig. 11 — Another example of ac detection scheme: A phase de bias with modulation or a large ac modulation alone.

In addition to the above-mentioned techniques, there is yet another one which is based on pulse operation (Fig. 12). The key element is the reciprocal, gated phase shifter which is an electro-optical gate. The advantage of this scheme lies in the fact that existing integrated optics techniques can be used, although these techniques can also be developed for the first two schemes.

Detailed analyses and implementation of these proposed modifications are subjects of future studies.

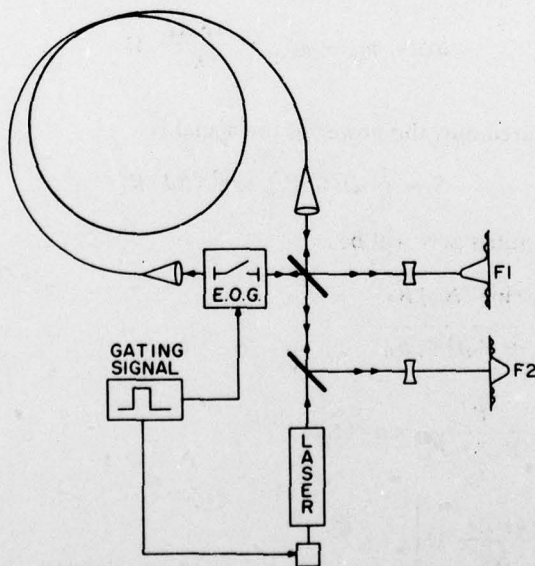


Fig. 12 — Another possible example of ac detection scheme: A reciprocal, gated-phase shifter, amplitude-detection technique.

SENSITIVITY LIMITS

Close investigation of Fig. 6 suggests the following question: Given a total loss rate and optical wavelengths, does there exist an optimum optical fiber length to produce a minimum detectable rotational rate? We also see from Eq. (33) that S/N is proportional to P_{cw} and, in turn, to P_0 , the laser output to the ring interferometer. Increasing P_0 will improve the S/N for a given L . However, there exists a limit beyond which the nonlinear optics effects, such as stimulated Brillouin scattering, will become dominant. If no upper limit is observed, fiber damage will result. Therefore, the practical sensitivity of a fiber ring interferometer is limited by spontaneous noises at low power and by stimulated noises at higher power. Because knowledge of these limits is extremely relevant in the preliminary design stage of a ring interferometer, inasmuch as the fiber length and power level are the important factors that determine the final package size and unit cost, we will assess these limits here.

Optimum Length and Minimum Detectable Rotational Rate at Low Power

We consider an improved version of the optical arrangement, in that a stable 90° dc phase bias has been introduced. With such an introduction, Eq. (8) for a single detector becomes

$$\begin{aligned} i_T &= D \left[\frac{1}{2} (P_{cw} + P_N) - \frac{1}{2} P_{cw} \cos \left(\Delta\phi + \frac{\pi}{2} \right) \right] \\ &= D \left[\frac{1}{2} (P_{cw} + P_N) + \frac{1}{2} P_{cw} \sin (\Delta\phi) \right], \end{aligned} \quad (34)$$

where

$$\Delta\phi = \phi_{cw} - \phi_{ccw} = \frac{4\pi RL}{\lambda c} \Omega.$$

If the dc term is filtered out, the power of the signal is

$$S = \frac{1}{4} D^2 G^2 P_{cw}^2 \sin^2 (\Delta\phi) R_L \quad (35)$$

and the quantum-noise-limited S/N will be

$$\begin{aligned} \frac{S}{N} &= \frac{\frac{1}{4} D^2 G^2 P_{cw}^2 \sin^2 (\Delta\phi) R_L}{q G^2 [D(P_{cw} + P_N)] R_L B_0} \\ &= \frac{1}{4} \left[\frac{\eta}{h\nu B_0} \right] \frac{P_{cw}^2}{P_{cw} + P_N} \sin^2 (\Delta\phi) \\ &= F(L) \sin^2 \left[\frac{4\pi RL}{\lambda c} \Omega \right], \end{aligned} \quad (36)$$

or, we can write

$$\sin (\beta \Omega L) = [(S/N) (1/F(L))]^{1/2},$$

whence

$$\Omega = \frac{1}{\beta L} \sin^{-1} [(1/F(L))(S/N)]^{1/2}. \quad (37)$$

The optimum fiber length L_0 is obtained by setting $(d\Omega/dL)_{L=L_0} = 0$ with $S/N = 1$.

Let $U \equiv [F(L)]^{-1/2}$; Eq. (37) then becomes (for $S/N = 1$)

$$\Omega = \frac{1}{\beta L} \sin^{-1} [U(L)]$$

and

$$\frac{d\Omega}{dL} = \frac{1}{\beta L^2} \left[-\sin U + \frac{L \frac{dU}{dL}}{\sqrt{1-U^2}} \right]. \quad (38)$$

By setting $(d\Omega/dL)_{L=L_0} = 0$, we obtain

$$U_0 = U(L_0)$$

and

$$\sin^{-1} U_0 = \frac{L_0}{\sqrt{1-U_0^2}} \frac{dU}{dL} \Big|_{L=L_0}. \quad (39)$$

Use of the distribution laws in Eq. (32) gives

$$U_0 = \left(\frac{4h\nu B_0}{\eta \Pi} \right)^{1/2} e^{\frac{1}{2}\alpha_T L_0} [1 + (A + B + C)L_0 + (B' + C')(e^{\alpha_T L_0} - e^{-\alpha_T L_0})]^{1/2} \quad (40)$$

and

$$\frac{dU}{dL} \Big|_{L=L_0} = U_0 \frac{\alpha_T}{2} \left[1 + H(L_0) \right], \quad (41)$$

where

$$H(L_0) = \frac{\left(\frac{A+B+C}{\alpha_T} \right) + (B'+C') (e^{\alpha_T L_0} + e^{-\alpha_T L_0})}{1 + (A+B+C)L_0 + (B'+C') (e^{\alpha_T L_0} - e^{-\alpha_T L_0})},$$

and

$$A = \frac{1}{5} \alpha_{SR}, \quad B = 0.2 \alpha_{SR}, \quad C = 0.2 \alpha_{SB}$$

$$B' = 0.1 \frac{\alpha_{SR}}{\alpha_T}, \quad C' = 0.1 \frac{\alpha_{SB}}{\alpha_T},$$

if the bare cladding fiber is used as an example. Appropriate corresponding values must be used for a mode-stripped fiber, but the procedure will remain the same. Substituting Eq. (40) and (41) into (39) gives a condition for the determination of L_0 for a given value of the param-

eter β . Equation (39) can only be solved numerically. We have carried out numerical solutions for the fused silica fiber discussed above for both $\lambda = 0.633 \mu\text{m}$ and $\lambda = 1.1 \mu\text{m}$. Numerical values of the other variables needed in the evaluation are given in Table 2. For a fiber coil of radius $R = 10 \text{ cm}$, numerical solutions are that (a) for $\lambda = 0.633 \mu\text{m}$, the optimum length $L_0 = 1.56 \text{ km}$, and (b) for $\lambda = 1.1 \mu\text{m}$, $L_0 = 14.3 \text{ km}$. The corresponding minimum rotational rates Ω_{\min} are $3.79 \times 10^{-8} \text{ rad/s}$ for $\lambda = 0.633 \mu\text{m}$ and $1.2 \times 10^{-8} \text{ rad/s}$ for $\lambda = 1.1 \mu\text{m}$. These are listed in Table 3.

As we expected, with due consideration of light scattering in fiber and 90° phase bias improvement, our results indicate less reason for optimism than found by in Vali and Shorthill [3]. However, we think that, with the implementation of any of the ac detection schemes and heavy mode stripping mentioned above, we may achieve an order of magnitude improvement in sensitivity.

Table 2 — Numerical Values of the Parameters used to Evaluate the Optimum Fiber Length (An Example)

Case	η	B_0 (Hz)	P_0 (mW)	α_1	C	Π (W)	$\left(\frac{4h\nu B_0}{\eta\Pi}\right)^{1/2}$
$\lambda = 0.633 \mu\text{m}$	0.5	1	2	0.5	0.5	1.25×10^{-4}	1.42×10^{-7}
$\lambda = 1.1 \mu\text{m}$	0.1	1	2	0.5	0.5	1.25×10^{-4}	2.4×10^{-7}

Table 3 — Quantum-Noise-Limited Performance*

λ (μm)	α_T (dB/km)	L_0 (km) Low-Power	Minimum Detectable Ω (deg/h)	
			Low-Power	High-Power
0.633	4	1.56	($P_0 = 2 \text{ mW}$) 0.0078	($P_0 = 81.2 \text{ mW}$) 0.0009
1.1	0.43	14.3	($P_0 = 2 \text{ mW}$) 0.0025	($P_0 = 14.4 \text{ mW}$) 0.0007

* 90° phase bias and fiber scattering; $R = 10 \text{ cm}$.

Effect of Stimulated Brillouin Scattering at High Power

Previous works [1,3,4] dealing with optical fiber ring interferometers and our discussions so far are limited to *linear* optics. However, the S/N will improve as we increase the laser power, hence the power coupled into the fiber, as evidenced by Eq. (36). The sensitivity in terms of the detectable rotational rate will also improve because $\Omega_{\min} = (\beta L_0)^{-1} \sin^{-1} U_0 \propto U_0$ for small U_0 . But $U_0 \propto \Pi^{-1/2} \propto P_0^{-1/2}$, hence $\Omega_{\min} \propto P_0^{-1/2}$. The upper limit for P_0 will be at a level where noises induced by stimulated processes become dominating and start to degrade the S/N and Ω_{\min} . These *nonlinear* optics effects will become more important as we reduce the total losses of optical fiber, for then more power input to these fibers would be available for stimulation.

The stimulated Raman and Brillouin scattering in an optical fiber have been investigated theoretically by R.G. Smith [56]. Based on the assumption of nondepleting pump beam and the criterion that the critical power is reached when the scattered power in the stimulated process is equal to the local pump power, Smith establishes that the backscattering stimulated Brillouin process requires the least pump power. Therefore, we shall concentrate on this process.

In order to present a discussion appropriate to the operation of fiber ring interferometers, we adopt a new criterion for the critical power. It states that, *for a chosen fiber length, the critical power is the input laser pump power for which the backscattered Stokes wave acquires a power level as high as the transmitted power of the beam coming from the other end of the fiber.* Let $P_p(0)$ be the pump power at the end $x=0$, $P_p(L)$ be that at $x=L$, $P_s(0)$, the backscattered Stokes wave emerging from $x=0$. Then, mathematically, the criterion translates into

$$P_s(0) = P_p(L) e^{-\alpha_r L}. \quad (42)$$

Since we have assumed symmetry in the CW and CCW directions, we can set $P_{(L)} = P_p(0)$ such that

$$P_s(0) = P_p(0) e^{-\alpha_r L}. \quad (43)$$

According to Smith [56], the backscattered stimulated Brillouin scattering has the lowest threshold and can be shown to follow the formula

$$P_s(0) = \frac{\sqrt{\pi}}{2} \left(\frac{\nu_s}{\nu_a} \right) (kT) (\Delta\nu_B) \sqrt{\frac{\gamma_0 P_p(0) \alpha_r}{A}} \times \int_0^L d\xi \left\{ \exp \left[-2\alpha_r \xi + \frac{\gamma_0 P_p(0)}{A \alpha_r} (1 - e^{-\alpha_r \xi}) \right] \right\}, \quad (44)$$

where ν_s and ν_a are the frequencies of the Stokes wave and the acoustic phonon, respectively, $\Delta\nu_B$ is the line width of the spontaneous Brillouin scattering, T is the absolute temperature of the fiber, γ_0 is the peak gain coefficient for the stimulated Brillouin process, A is the core cross-sectional area. This expression is applicable for all $\alpha_r L$, since we have used Smith's expression for full gain given by his Eq. (B5). Substitution of (44) into Eq. (43) gives a final equation for evaluating the critical input pump power when all the other parameters are known.

Two cases have been evaluated: namely, $\lambda = 0.633 \mu\text{m}$ and $\lambda = 1.1 \mu\text{m}$. In doing so, we have ignored the frequency shift of the scattered light and set $\nu_s = \nu_{\text{laser}}$. We also arbitrarily take $L = L_0$, which are determined from low-power calculations. Other values used in the evaluation are listed in Table 4.

Results show that, for the case $\lambda = 0.633 \mu\text{m}$, the critical input pump power $P_p(0) = 10$ mW, and for $\lambda = 1.1 \mu\text{m}$, $P_p(0) = 1.8$ mW. In terms of the laser output power ($P_0 = P_p(0) / [1/2(1-\alpha_1)C]$), we have $P_0 = 1.8 \text{ mW} \times 8 = 14.4 \text{ mW}$ for $\lambda = 1.1 \mu\text{m}$ and $P_0 = 81.2 \text{ mW}$ for $\lambda = 0.633 \mu\text{m}$.

Based on our criterion, the quantum-limited S/N ratio, according to Eq. (36), with $P_N = P_{\text{cw}}$, is given by

$$\left(\frac{S}{N} \right) = \frac{1}{8} \frac{\eta P_{\text{cw}}}{h \nu B_0} \sin^2 (\beta L \Omega) \quad (45)$$

where we have set $P_s(0) = P_N = P_{cw}$. Setting $S/N = 1$, the minimum detectable rotational rate is given by

$$\Omega_{\min} = \left(\frac{8h\nu B_0}{\eta P_p(0)} \right)^{1/2} \frac{1}{\beta} \frac{e^{\frac{1}{2}\alpha_f L}}{L}, \quad (46)$$

where the approximation $\sin^{-1}x \approx x$ for small x , and $P_s(0) = P_{cw} = P_p(0)e^{-\alpha_f L}$ is assumed. As an example, let us consider the same ring interferometers used for low power rates as above. Our numerical calculations show that, for the case $\lambda = 0.633 \mu\text{m}$, $\Omega_{\min} = 4.44 \times 10^{-9} \text{ rad/s}$, or $9.16 \times 10^{-4} \text{ deg/h}$, whereas for $\lambda = 1.1 \mu\text{m}$, $\Omega_{\min} = 3.35 \times 10^{-9} \text{ rad/s}$, or $6.9 \times 10^{-4} \text{ deg/h}$. These values are listed in the last column of Table 3. It is of interest to compare these with the counterparts for the low-power cases: For $\lambda = 0.633 \mu\text{m}$, the high-power performance in rotational rate sensing has about 88% improvement over the low-power value. For $\lambda = 1.1 \mu\text{m}$, we gain about 72% improvement. The optimum fiber length L_0 , which gives Ω_{\min} for $S/N = 1$, can be determined from Eq. (46). The result is that $L_0 = 2/\alpha_f$. This condition still applies if we neglect all the scattered light components ($P_N = 0$), and it is different from the condition $L_0 = 0.87/\alpha_f$ as given by Ref. 3.

What is the sensitivity for the ideal case? This question may become relevant when the state of fiber development reaches a high level of perfection whereby the scattered light is insignificant and when *ultrastable dc bias and ac modulation techniques* can be implemented.

In the absence of scattered light, the ideal S/N for the dc detection scheme is

$$\frac{S}{N} = \frac{1}{4} \frac{\eta P_{cw}}{h\nu B_0} \sin^2(\beta L \Omega) \quad (47)$$

whence (for $S/N = 1$)

$$\Omega_{\min} = \left(\frac{4h\nu B_0}{\eta P_p(0)} \right)^{1/2} \frac{e^{\frac{1}{2}\alpha_f L}}{\beta L}. \quad (48)$$

Comparing with (46), we see that the minimum detectable rotational rate in the ideal case is a factor $1/\sqrt{2}$ lower than the high-power case. If the differential scheme is used, the ideal minimum detectable rotational rate is a factor of one-half lower. For the heterodyne case, we would expect a factor of $1/(2\sqrt{2})$ lower.

CONCLUDING REMARKS

Optical-fiber, ring interferometers and their variants can also be used for the detection of other physical parameters besides being highly sensitive rotational rate transducers. Physical effects such as the acoustic pressure field, stress distributions in composite materials, the temperature field, and magnetic fields can be detected through the optomechanical, magneto-optical properties of the fiber materials. Acoustic pressure field measurements have been demonstrated [5], and other effects are currently under evaluation in our laboratory. The present sensitivity analysis will certainly facilitate the evaluation.

Up to now, our discussions have not included the depolarization effects in a single-mode fiber. In certain applications, such as stress measurements or temperature measurements, the

Table 4 — Values of the Parameters Used for the Evaluation of the Critical Pump Power in Equations (43) and (44).

λ (μm)	L (cm)	α_T (cm^{-1})	k (J/K)	T (K)	ν_s (Hz)	ν_a (Hz)	$\Delta\nu_B$ (Hz)	γ_0 (cm/W)	A (cm^2)
0.633	1.56×10^5	9.24×10^{-6}	1.38×10^{-23}	293	4.47×10^{14}	2.73×10^{10}	8×10^7	5.36×10^{-9}	2.827×10^{-7}
1.1	1.43×10^6	9.95×10^{-7}	1.38×10^{-23}	293	2.73×10^{14}	1.64×10^{10}	5×10^7	3×10^{-9}	2.827×10^{-7}

Table 5 — Comparisons of Single-Axis Gyroscope Performance

Gyroscope	Sensitivity (deg/h)	Cost (\$)	Cost (Projected) (\$)	Weight (lb)	Power (W)	Moving Parts	Warm-up Time	Sensitive to Acceleration	Sensitive to Temperature
Litton PS500 (in use, 1977)	0.003	10,000		8	50	Yes	2-3 min	Yes	Yes
Honeywell GG1300 (NWC TM2855, July 1976)	0.01	15,000	3,000	5	6	No (dither)	2s	No	No
Fiber Gyro (anticipated)	0.003— 0.0005	20,000	1,500	3	3	No	Fast	Possibly	No

polarization state of the optical beam in the fiber can be used to our advantage; but, in ring interferometers for rotational rate measurements, if a linearly polarized beam is used, depolarization will cause signal level reduction, (a factor of 2 for complete depolarization). Therefore, the effect of depolarization due to uncontrolled nonreciprocal changes in the fiber should be investigated. Nonlinear effects with pump depletion should also be investigated.*

Our analysis of the sensitivity has shown that when laser input power is low, spontaneous noises are important, and they degrade the S/N ratio. The higher the fiber loss, the stronger the scattered light, hence the noise power. However, the level of degradation may be reduced considerably if a proper mode stripper can successfully remove these cladding-guided, scattered components. We can expect two orders of magnitude in improvement. But, when the input power is increased to above certain levels, the nonlinear, stimulated scattering will dominate. The power level beyond which nonlinear optics effects are important is lower when optical fiber of lower loss is used. On the other hand, sensitivity will increase as the square root of power. Our analysis shows that, when the stimulated Brillouin scattering is taken as the sole source of noise, the gyro sensitivity is better than that of the low-power case. We conclude that, in pursuant to the low-loss, single-mode fiber development, the fiber-ring interferometer should operate with the highest possible input power.

Because the optical fiber technology, light sources such as laser diodes and detectors are currently under intense research and development for optical fiber communications systems, the promising use of optical fiber as the transducer can, in fact, be tied to the advancement in that field. Researchers in optical fiber communications systems have pointed out the clear advantage of operating the systems in the infrared [49,56]. From the point of view of scattering noise, ring interferometers should also follow this trend. What seems to be the limitation today may soon be removed tomorrow. Our optimistic viewpoint is supported by the favorable comparison of the ring interferometer with a specific, well-developed mechanical gyro and an advanced ring laser gyro. This is shown in Table 5.† We conclude that ring interferometers as fiber gyros can soon be the alternative to ring-laser gyros in certain applications. The ultimate sensitivity as a gyro is anticipated to be even higher than the ring laser gyro.

ACKNOWLEDGMENT

This research was supported by the Naval Air Systems Command. The authors are much obliged to Dr. Steve Hanley for his help in evaluating the critical input pump power based on Eqs. (43) and (44).

REFERENCES

1. R.B. Brown, NRL Memorandum Report 1871, March 1968, Naval Research Laboratory, Washington, D.C. 20375, pp. 19-22.
2. Single-mode optical fiber with loss below 1 dB/km between $\lambda = 1.0 \mu\text{m}$ and $1.1 \mu\text{m}$ has been reported by A. Kawana, T. Miyashita, M. Nakahara, M. Kawachi, and T. Hosaka,

*The case with pump depletion has been worked out most recently by J. Au Yeung and A. Yariv for the stimulated Raman scattering in an optical fiber. IEEE J. Quantum Electron. QE-14, p. 347 (1978)

†In developing this table, we were benefited by discussions with D. Alberez of Naval Ocean Systems Command and with D. Klenin, then with Naval Air Systems Command.

- Electron. Lett. **13**, p. 188 (1977); also, *Tech. Digest*, pp. 275-278, 1977 International Conference on Integrated Optics and Optical Fiber Communication, July 18-20, 1977, Tokyo, Japan.
3. V. Vali and R.W. Shorthill, *Appl. Opt.* **15**, 1099 (1976).
4. V. Vali and R.W. Shorthill, *Appl. Opt.* **16**, 290 (1977).
5. J.A. Bucaro, H.D. Dardy, and E.F. Carome, *Appl. Opt.* **16**, p. 1761 (1977).
6. G.E. Moss, L.R. Miller, and R.L. Forward, *Appl. Opt.* **10**, 2495 (1971).
7. R.J. Post, *Rev. Mod. Phys.* **39**, 475 (1967).
8. W.R.C. Rowley, *IEEE Trans. IM-15*, 146 (1966).
9. J. Shamir, R. Fox, and S.G. Lipson, *Appl. Opt.* **8**, 103 (1969).
10. See the review article: "Light Beating Spectroscopy," by H.Z. Cummins and H.L. Swinney in *Progress in Optics*, Ed. Emil Wolf. Vol. VIII, North-Holland (1970).
11. W.K. Platt, *Laser Communication Systems*, John Wiley and Sons (1969). Chapter 8 and 10.
12. H. Melchior, *J. Luminescence* **7**, 390-414 (1973).
13. A.R. Tynes, A. David Pearson, and D.L. Bisbee, *J. Opt. Soc. Amer.* **61**, 143-153 (1971).
14. Yu. M. Blagidze, M.I. Dzhibladze, A.M. Mestvirishvili, M.E. Perel'man, G.M. Rubinsh-
tein, Sov. and V.S. Chagulov, *Sov. J. Quant. Electron.* **3**, 335-336 (1974).
15. S.S. Budrin, A.V. Goncharov, A.V. Samuilov, and L.M. Kuchikyan, *Sov. J. Opt. Technol.*
44, 12-14 (1977).
16. See, e.g., A.W. Snyder and D.J. Mitchell, *Electron. Lett.*, **10**, p. 11 (1974), K. Peter-
mann, *Opt. and Quantum Electron.* **9**, 167 (1977); and D.F. Nelson, D.A. Kleinman, and
K.W. Wecht, *Appl. Phys. Lett.* **30**, 94 (1977).
17. R.B. Dyott and J.R. Stern, *Electron. Lett.* **7**, 624-625 (1971).
18. F.P. Kapron, R.D. Maurer, and M.P. Teter, *Appl. Opt.* **11**, 1352 (1972).
19. W.M. Hubbard, *Appl. Opt.* **11**, 2495-2501 (1972).
20. D. Gloge, *Appl. Opt.* **13**, 249 (1974).
21. D. Gloge, *Appl. Opt.* **10**, 2252 (1971).
22. J. Stone, *Appl. Opt.* **12**, 1824-1827 (1973).

LIN AND GIALLORENZI

23. J. Schroeder, R. Mohr, P.B. Macedo, and C.J. Montrose, *J. Amer. Ceram. Soc.* **56**, 510-514 (1973).
24. E.G. Rawson, *Appl. Opt.* **11**, 2477 (1972).
25. M.H. Reeve, M.C. Brierley, J.E. Midwinter, and K.I. White, *Opt. and Quantum Electron.* **8**, 39-42 (1976).
26. E.G. Rawson, *Appl. Opt.* **10**, 2778 (1971).
27. R.D. Maurer, *J. Chem. Phys.* **25**, 1206-1209 (1956).
28. E.G. Rawson, *J. Opt. Soc. Amer.* **62**, 1284 (1972).
29. D. Marcuse, *Bell Systems Tech. J.* **48**, 3233-3242 (1969).
30. A.W. Snyder, *IEEE Trans. MTT-18*, 608 (1970).
31. E.G. Rawson, *Appl. Opt.* **13**, 2370 (1974).
32. D. Marcuse, *Appl. Opt.* **14**, 3021 (1975).
33. H.F. Mahlein, *Appl. Phys.* **13**, 137-140 (1977).
34. D.B. Keck, R.D. Maurer and P.C. Schultz, *Appl. Phys. Lett.* **22**, 307 (1973).
35. D.A. Pinnow, T.C. Rich, F.W. Ostermayer, Jr., and M. DiDomenico, Jr., *Appl. Phys. Lett.*, **22**, 527 (1973).
36. I.L. Fabelinskii, *Molecular Scattering of Light*, Plenum Press, New York, 1968.
37. T.C. Rich and D.A. Pinnow, *Appl. Phys. Lett.* **20**, 264 (1972).
38. M. Balkanski, R.C.C. Leite, and S.P.S. Porto, Eds., *Proc. 3rd Intl. Conf. Light Scattering in Solids*, July 25-30, 1975 (John Wiley & Sons, New York, 1976), Chap. X, p. 621-630; Chap. XI, p. 673-687.
39. T.C. Rich and D.A. Pinnow, *Appl. Opt.* **13**, 1376 (1974).
40. E.M. Dianov, A.A. Manenkov, and A.I. Ritus, *Sov. J. Quantum Electron.* **7**, 841 (1977).
41. I.H. Malitson, *J. Opt. Soc. Amer.* **55**, 1205 (1965).
42. B. Brixner, *J. Opt. Soc. Amer.* **57**, 674 (1967).
43. L.D. Landau and E.M. Lifshitz, *Electrodynamics of Continuous Media*, English translation by J.B. Sykes and J.S. Bell, Pergamon Press, New York, 1960, pp. 331-337.

NRL REPORT 8250

44. See, e.g., F.J. Sansalone, *Appl. Opt.* **10**, 2329 (1971); and J.A. Wunderlich and L.G. Deshazer, *Appl. Opt.* **16**, 1584 (1977).
45. See, e.g., H. Gamo, S.S. Chuang, and R.E. Grace, *IEEE J. Quantum Electron.* **QE-3**, 243 (1967); and S.S. Chuang and H. Gamo, *J. Opt. Soc. Amer.* **59**, 505 (1969).
46. For a good review of magneto-optical materials, see W.G. Tabor, "Magneto-Optic Materials," Chapter D4 of *Laser Handbook*, Eds. F.T. Arecchi and E.O. Schulz-DuBois, North-Holland, 1972.
47. H. Takeuchi, S.I. Ito, I. Mikami, and S. Taniguchi, *J. Appl. Phys.* **44**, 4789 (1973).
48. J.J. Hsieh, J.A. Rossi, and J.P. Donnelly, *Appl. Phys. Lett.* **28**, 709 (1976).
49. T. Kimura and K. Daikoku, *Opt. and Quantum Electron.* **9**, 33-42 (1977).
50. K.M. van Vliet, *Appl. Opt.* **6**, 1145 (1967).
51. A. van der Ziel, *Proc. IEEE* **58**, 1178 (1970).
52. J. Hanlon and S.F. Jacobs, *Appl. Opt.* **6**, 577 (1967).
53. C. Smit, C. Th. J. Alkemade, and W.F. Muntjewerff, *Physica* **29**, 41 (1963).
54. J.J. Brophy, *Phys. Rev.* **166**, 827 (1968) and *J. Appl. Phys.* **41**, 2913 (1970); W.E. Purcell, *J. Appl. Phys.* **43**, 2890 (1972).
55. R.C. LeCraw, *IEEE Trans. MAG-2*, 304 (1966); C.D. Mee, *Contemp. Phys.* **8**, 385 (1967); M.V. Chetkin and V.S. Solomatin, *Soviet Phys. — Solid State* **8**, 2708 (1967); V.V. Danilov, I.A. Derygin, I.S. Melishchuk, and V.D. Tron'ko, *Radio Eng. Electron. Phys.* **15**, 314 (1970); and H. Takeuchi, I. Mikami, and S. Taniguchi, *J. Appl. Phys.* **46**, 3626 (1975).
56. R.G. Smith, *Appl. Opt.* **11**, 2489 (1972).